On the Continuous-Time Model for Nonlinear-Memory Modeling of RF Power Amplifiers

Edouard Ngoya, *Member, IEEE*, Christophe Quindroit, and Jean Michel Nébus

***Abstract*—The RF front-end in modern communication systems is faced with variable envelope and large bandwidth signals (including desired signals and large interferers), which require the behavioral model of the amplifying unit (either in Tx or Rx) to accurately account for nonlinear memory effects. Important advancements have been made on the subject; however it is still challenging to derive a model that performs equally well with all possible input stimuli. This paper gives a concise overview of the recent developments that have been made on the continuous-time modeling approach for the behavioral modeling of nonlinear memory in power amplifiers, as opposed to the explicit discrete-time modeling approach.**

***Index Terms*—Behavioral modeling, nonlinear integral model, nonlinear memory, RF amplifier.**

I. Introduction

THE behavioral modeling of the power amplifier (PA) has lately been the subject of numerous studies, especially in the context of solid-state amplifiers and mobile communication systems [1], [2]. Accurate, simple to extract and fast execution behavioral models of PA are necessary for the exploration and optimization of the communication system performance, as well as for the PA linearization design. It must also be noted that even though the modeling focus is usually on the transmit PA, an accurate model is also necessary for the receive low-noise amplifier (LNA), as this is frequently made to work in a saturated regime by large peak-to-average-ratio orthogonal frequency division multiplexing (OFDM) signals and large spurious interferer signals.

It is now well understood that the RFPA is affected by two types of memory: short-term memory (STM), primarily caused by matching networks and transit time within the transistors (i.e., in-band frequency dispersion), and long-term memory (LTM), due to biasing circuits, automatic gain control (AGC) circuits, transistor self-heating and trapping effects (i.e., out-band low-frequency dispersion). It has also been evidenced that the LTM causes the most critical signal distortion, as it is harder to precompensate using usual predistortion techniques [3].

Manuscript received May 12, 2009; revised July 30, 2009. First published November 13, 2009; current version published December 09, 2009.

The authors are with XLIM, UMR-CNRS 6172, University of Limoges, Limoges 87060, France (e-mail: edouard.ngoya@xlim.fr).

Color versions of one or more of the figures in this paper are available online at http://ieeexplore.ieee.org.

Digital Object Identifier 10.1109/TMTT.2009.2033297

A number of approaches and variations have been proposed for designing the PA model, which can be divided into two categories: the explicit-discrete-time model [4]–[18] and the continuous-time model [19]–[39] approaches.

The explicit-discrete-time model approach is the most direct and common one, it directly fits the discrete-time simulation environment where the model is to be used. This comprises the popular memory-polynomial model [8]–[13], its more general time-series variant [14]–[18] and the discrete Volterra series model [4]–[7]. The approach however suffers a number of well-known drawbacks, mostly the difficulty of the selection of the number of delay taps and their time distribution. This affects the model learning capabilities and is a source for overfitting issues, especially in the presence of short and long time constants.

On the other hand, the continuous-time model is an indirect approach to the ultimate discrete-time implementation; it tends to mimic the well-established device compact modeling process. First, an equivalent network is postulated as a collection of linear/nonlinear integro-differential equations from device physics and/or empirical observations. Second, conveniently chosen and usually simple stimuli are used to identify the kernels of the integro-differential equations. Finally a numerical integration scheme is employed to digitize the identified model equations. The approach comprises the so-called two-box, three-box, and parallel Hammerstein–Wiener models [19]–[21], the polyspectral models [22], and the nonlinear-integral models [23]–[39]. This approach has the advantage that the number of delay taps and their time distribution are not fixed *a priori* for all input signals, but are automatically adjusted from the extracted integro-differential kernels and the incoming input signal speed.

In turn the difficulty on the continuous-time model approach lies in devising a good theory for constructing an equivalent network sufficiently representative of the PA internal dynamics. We may here distinguish two categories of models, which we will term single-memory-path (SMP) model and two-memory-path (TMP) model that differ according to whether or not the equivalent network has separate branches for STM and LTM mechanisms.

The SMP model [19]–[27] is the most direct one; the PA is represented by some network, usually a cascaded and/or parallel association of linear filters, memoryless nonlinearities and/or Volterra kernels, whose transfer functions (kernels) are to be identified from a specific regression procedure. In this case, STM and LTM contributions are not distinguished and hence captured as an average effect. The identification process thus

tends to be ill-conditioned, limiting the generalization property of the model. A comprehensive survey of the various works on the approach may be found in the review by Pedro and Maas [2].

The TMP model approach tries to resolve the aforementioned limitation by getting more insight into the memory mechanism, dissociating the contributions of the two types of effects. The model is then represented by an equivalent network comprising distinct branches for STM and LTM dynamics. A few works have been carried out on this direction in the last decade [28]–[39] since the introduction by Bosch and Gatti [3] in 1989. This paper extends the work in [39]; it gives a synthesis of the previous works and theoretical details on the recent developments constituting, from our perspective, the state-of-the-art in PA continuous-time models.

In the following, Section II introduces and clarifies the TMP model concept from [3], [28]–[39], and then identifies the two model topologies (the feedback (FB) and feed-forward (FF) topologies) arising from this concept. In Section III, we investigate the most common topology (i.e., FF topology), and identify a systematic limitation in the original TMP model concept, especially for the modeling of PAs with IMD asymmetries. In Section IV, a new state variable is introduced in the concept to resolve the issue. Section V examines the theory for the FB model topology parameters extraction. Section VI addresses the numerical implementation issues of these continuous-time models and Section VII shows an application example and examines the implementation efficiency and modeling accuracy of the proposed solutions. Finally, Appendices I-A–I-E give details of model equation derivations and step-by-step algorithms for the model extraction and implementation.

II. Two-Memory Path Model

At the system level, the basic assumption is that signal $x(t)$ at any port can be expressed as a band limited modulated signal

$$x(t) = \Re e(\hat{x}(t) \cdot e^{j\omega_0 t}) \tag{1}$$

where $\hat{x}(t)$ and ω_0 are, respectively, the complex envelope (the modulation) and the carrier. For modeling the PA, we need to identify the relationship between the complex envelope input $\hat{x}(t)$ and the output $\hat{y}(t)$. To that end Mazière *et al.* [34], following similar considerations by Bosch *et al.* [3], Meghdadi *et al.* [28], Vuolevi *et al.* [29], Asbeck *et al.* [30], Draxler *et al.* [31], Pedro *et al.* [32], Boumaiza *et al.* [33], Kenney *et al.* [36], Mazeau *et al.* [37], and Verspecht *et al.* [38] proposed the two-memory-path model topology depicted in Fig. 1. This topology tends to mimic the two basic memory routes within the PA circuit. The PA output is modeled as a short-term-memory response that gets modulated by a long-term response in a FB system. An important assumption in these works is that the long-term modulation is solely driven by the time varying amplitude of the envelope, i.e., $|\hat{x}(t)|$, which we will later show is not necessarily true.

In the FB model structure, Fig. 1, the STM path is intended to capture the principal dynamics of the PA, i.e., the one responsible for the amplification and bandpass filtering effects. When a variable envelope signal goes along this path, the short-term nonlinearity generates a low frequency signal that is fed back to the input following an LTM path. This LTM dynamics is itself nonlinear; it can be seen as a slow modulation of the dc quiescent point of the amplifier, at the rate of bias network charging/discharging, device self-heating or eventual trapping effects. These memory mechanism interactions are sketched in the artistic view Fig. 2.

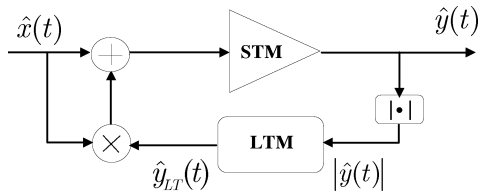

Fig. 1. Two-memory-path FB model topology.

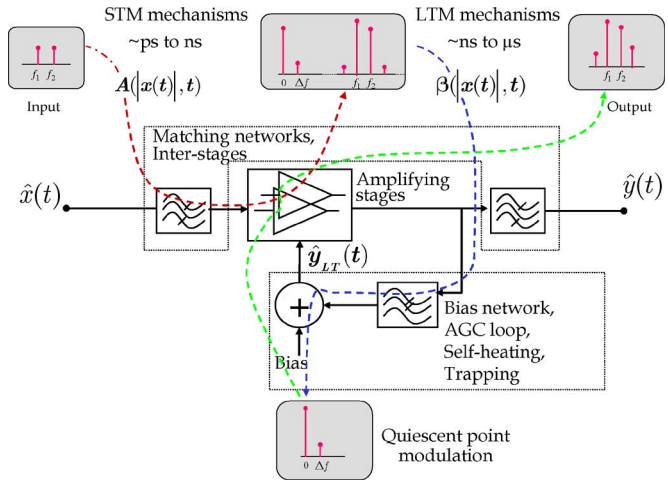

Fig. 2. PA two-memory-path mechanism interaction.

Some of the works, especially [31], [35], [37], have tried to dissociate the self-heating effects from the other LTM mechanisms. This dissociation, however, is not easily accomplished since the time constants of the various mechanisms fall practically in the same range. Moreover, as shown in [37], an effective characterization of heat generation and dissipation in the PA is hardly doable with conventional measurement techniques but requires a complex 3-D finite element simulation of the amplifier chip, package layers, and heat sink that unfortunately is not easily affordable for most designers.

The method proposed in this work does not make a distinction between the LTM mechanisms; these are considered as a whole, as is indicated in Fig. 2.

Now let $\hat{x}(t), \hat{y}(t)$ and $\hat{y}_{\mathrm{LT}}(t)$ be the input, output, and FB signals in Figs. 1 and 2, respectively. For the purpose of illustration, if we assume that the complex signals $\hat{x}(t)$ and $\hat{y}(t)$ are both nonzero at any time instant t, then without loss of generality, we have that the STM and LTM paths are characterized by a time varying complex gain $A(|\hat{x}(t)|, t)$ and a FB coefficient $\beta(|\hat{x}(t)|, t)$, respectively, so that we may write the following:

$$\begin{aligned} \hat{y}(t) &= A(|\hat{x}(t)|, t) \cdot (1 + \hat{y}_{\mathrm{LT}}(t)) \cdot \hat{x}(t) \\ \hat{y}_{\mathrm{LT}}(t) &= \beta(|\hat{x}(t)|, t) \cdot |\hat{y}(t)|. \end{aligned} \tag{2}$$

Note that the equivalent STM path gain and LTM path FB coefficient above are both invariant with the input signal phase

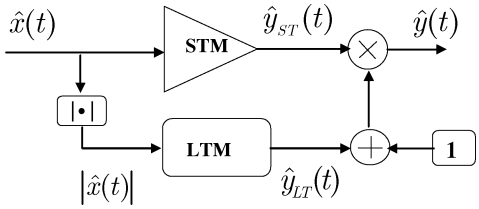

Fig. 3. Two-memory-path FF model topology.

since the PA is supposed to be a time-invariant system [24], [25]. Factoring (2), the model output takes the canonical FB loop equation

$$\hat{y}(t) = \frac{A(|\hat{x}(t)|,t)\cdot\hat{x}(t)}{1 - A(|\hat{x}(t)|,t)\cdot\beta(|\hat{x}(t)|,t)\cdot\frac{|\hat{y}(t)|\hat{x}(t)}{\hat{y}(t)}}. \quad (3)$$

Now, if we consider an assumption that the open-loop gain $A(|\hat{x}(t)|,t)\cdot\beta(|\hat{x}(t)|,t)\cdot|\hat{y}(t)|\hat{x}(t)/\hat{y}(t)$ is small compared to 1, then the model output can be approximated as follows:

$$\hat{y}(t) \simeq (1 + M(|\hat{x}(t)|,t)\cdot|\hat{x}(t)|)\cdot A(|\hat{x}(t)|,t)\cdot\hat{x}(t) \quad (4.1)$$

where

$$M(|\hat{x}(t)|,t) = A(|\hat{x}(t)|,t)\cdot\beta(|\hat{x}(t)|,t)\cdot\frac{|\hat{y}(t)|}{|\hat{x}(t)|}\frac{\hat{x}(t)}{\hat{y}(t)}. \quad (4.2)$$

In (4) it is understood that the phase angle ratio between $\hat{y}(t)$ and $\hat{x}(t)$ is also a function of $|\hat{x}(t)|$ and invariant to phase for sake of system time-invariance. It is then apparent from (4) that under the assumption of relatively low long-term memory effects, the FB topology of the model, Fig. 1, may be approximated by a FF structure Fig. 3.

In the following, we will first investigate the FF topology because of its relative simplicity and then extend the derivations to the FB topology.

III. FF Model Topology

Considering the structure in Fig. 3, we observe that STM and LTM effects can be easily de-embed from the system response as follows. Indeed in the above TMP topologies, when the input amplitude $|\hat{x}(t)|$ is time invariant, any time variation in the output envelope is due only to the STM mechanisms. Hence the STM contribution may be easily identified from a single-tone continuous wave (CW) stimulus, with a frequency sweep in the bandwidth. Once the STM contribution has been identified, the LTM contribution can then be probed with a stimulus exhibiting time-varying amplitude.

More precisely, the experiments carried out in the previous works [24]–[27], [34], [35] have shown that both the STM and the LTM dynamics, when considered individually, are efficiently described by a nonlinear integral model as follows:

$$\hat{y}_{\rm ST}(t) = \int_0^\infty \hat{h}_{\rm ST}(|\hat{x}(t-\tau)|,\tau)\hat{x}(t-\tau)d\tau \quad (5.1)$$

$$\hat{y}_{\rm LT}(t) = \int_0^\infty \hat{h}_{\rm LT}(|\hat{x}(t-\tau)|,\tau)|\hat{x}(t-\tau)|d\tau. \quad (5.2)$$

Hence, the model output writes

$$\hat{y}(t) = (1 + \hat{y}_{\rm LT}(t))\hat{y}_{\rm ST}(t). \quad (5.3)$$

We thus define the time-varying frequency-domain (TVFD) kernels associated with the STM and LTM nonlinear impulse responses in (5) as

$$\hat{H}_{\rm ST}(|\hat{x}(t)|,\omega) = \int_0^\infty \hat{h}_{\rm ST}(|\hat{x}(t)|,\tau)e^{-j\omega\tau}d\tau \quad (6.1)$$

$$\hat{H}_{\rm LT}(|\hat{x}(t)|,\omega) = \int_0^\infty \hat{h}_{\rm LT}(|\hat{x}(t)|,\tau)e^{-j\omega\tau}d\tau. \quad (6.2)$$

As explained above, to identify the TVFD kernels, we will first drive the PA with a single-tone CW signal $x(t) = \Re e(\hat{X}_0\cdot e^{j(\omega_0+\Omega)t})$, so that the input envelope has constant-amplitude and linear time-varying phase, i.e.,

$$\hat{x}(t) = \hat{X}_0 e^{j\Omega t}. \quad (7)$$

Because of the bandpass property of the PA, the PA output signal is also a constant amplitude envelope signal at the input frequency, which writes

$$\hat{y}(t) = \hat{Y}_0(\hat{X}_0,\Omega)e^{j\Omega t}. \quad (8)$$

Accounting of (7) in (5.3) we find that the model output signal expresses

$$\hat{y}(t) = (1 + \hat{H}_{\rm LT}(|\hat{X}_0|,0))\cdot\hat{H}_{\rm ST}(|\hat{X}_0|,\Omega)\cdot\hat{X}_0 e^{j\Omega t}. \quad (9)$$

Note that because the model kernels are invariant to the input signal phase, the complex amplitude $\hat{X}_0$ can be given an arbitrary phase in the experiment. Henceforth, to simplify the notation, we will consider that $\hat{X}_0$ is real and positive, so that we may substitute $|\hat{X}_0|$ with $\hat{X}_0$.

Now equating (9) and (8), we find

$$(1 + \hat{H}_{\rm LT}(\hat{X}_0,0))\cdot\hat{H}_{\rm ST}(\hat{X}_0,\Omega) = \frac{\hat{Y}_0(\hat{X}_0,\Omega)}{\hat{X}_0}. \quad (10)$$

By virtue of the postulated long-term memory generation principle, we observe that $\hat{H}_{\rm LT}(\hat{X}_0,0)$ must be zero, because a constant amplitude signal cannot generate a modulation stimulus. Hence, we identify the STM kernel simply as the ratio of the PA output signal to the input

$$\hat{H}_{\rm ST}(\hat{X}_0,\Omega) = \frac{\hat{y}(t)}{\hat{x}(t)} = \frac{\hat{Y}_0(\hat{X}_0,\Omega)}{\hat{X}_0}. \quad (11)$$

The input amplitude $\hat{X}_0$ and frequency offset Ω are then swept throughout the operating input amplitude range and frequency bandwidth, respectively, in order to fully characterize the PA. The STM kernel $(\hat{H}_{\rm ST}(\hat{X}_0,\Omega))$ thus corresponds to the so-called AM-AM, AM-PM characteristic of the PA, as a function of the input frequency.

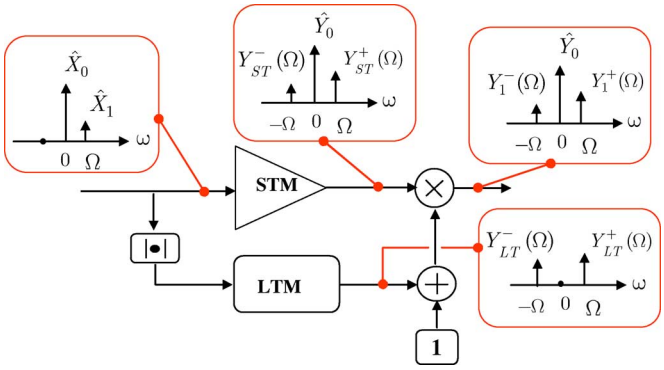

Fig. 4. FF LTM kernels extraction bench.

For identifying the LTM kernel ($\hat{H}_{\rm LT}(|\hat{x}|,\Omega)$), we drive the PA with the following two-tone stimulus: a large-amplitude tone and a small-amplitude tone CW signal

$$x(t) = \Re e\left(\hat{X}_0 \cdot e^{j\omega_0 t} + \hat{X}_1 \cdot e^{j(\omega_0+\Omega)t}\right). \tag{12.1}$$

This yields a time-varying envelope composed of a small-signal ac envelope on top of a large dc envelope

$$\hat{x}(t) = \hat{X}_0 + \hat{X}_1 e^{j\Omega t}, |\hat{X}_1| \gg 1. \tag{12.2}$$

With this excitation, the spectrum content of the signals observed at the PA output and at the model internal nodes are thus as illustrated in Fig. 4.

Applying (12) to (5), as described in Appendix I-A, we finally find the differential equation for solving $\hat{H}_{\rm LT}(\hat{X}_0,\Omega)$ as follows:

$$\begin{aligned}
\hat{H}_{\rm LT}(\hat{X}_0,\Omega) + \hat{X}_0\frac{\partial \hat{H}_{\rm LT}(\hat{X}_0,\Omega)}{\partial \hat{X}_0} &= 2\frac{Y^{+}_{\rm LT}(\hat{X}_0,\Omega)}{\hat{X}_1}\\
\hat{H}_{\rm LT}(\hat{X}_0,-\Omega) + \hat{X}_0\frac{\partial \hat{H}_{\rm LT}(\hat{X}_0,-\Omega)}{\partial \hat{X}_0} &= 2\frac{Y^{-}_{\rm LT}(\hat{X}_0,\Omega)}{\hat{X}_1}\\
\hat{H}_{\rm LT}(\hat{X}_0,-\Omega) + \hat{X}_0\frac{\partial \hat{H}_{\rm LT}(\hat{X}_0,-\Omega)}{\partial \hat{X}_0} &= 2\frac{Y^{+}_{\rm LT}(\hat{X}_0,-\Omega)}{\hat{X}_1}\\
\hat{H}_{\rm LT}(\hat{X}_0,\Omega) + \hat{X}_0\frac{\partial \hat{H}_{\rm LT}(\hat{X}_0,\Omega)}{\partial \hat{X}_0} &= 2\frac{Y^{-}_{\rm LT}(\hat{X}_0,-\Omega)}{\hat{X}_1}.
\end{aligned} \tag{13}$$

A close observation of (13) however shows that this is an overdetermined system of four equations in the two unknowns $\hat{H}_{\rm LT}(\hat{X}_0,\Omega)$ and $\hat{H}_{\rm LT}(\hat{X}_0,-\Omega)$. This has a unique solution only if the synchronous and anti-synchronous components of the LTM are identical by stimulus conjugation, i.e., if the following condition is verified:

$$\begin{aligned}
Y^{-}_{\rm LT}(\hat{X}_0,-\Omega) &= Y^{+}_{\rm LT}(\hat{X}_0,\Omega)\\
Y^{+}_{\rm LT}(\hat{X}_0,-\Omega) &= Y^{-}_{\rm LT}(\hat{X}_0,\Omega).
\end{aligned} \tag{14}$$

In the previous works [27], [34], [35], the condition (14) has been implicitly assumed, so that two of the equations were not taken into account; this however is not valid for all circuits. Experimentations carried out on a number of circuits have shown that the equality (14) is not verified, especially at large frequency offset Ω, as we will see in the application example Section VII.

The indetermination in (13) is actually the consequence of an insufficiency in the assumption that the LTM is solely driven by the time varying amplitude of the envelope, i.e., $|\hat{x}(t)|$. In Section V, we will introduce a new state variable to remove the indetermination and get a well conditioned identification process.

IV. Modified FF Model Topology

We have seen that the principal generating assumption of the TMP model topology (see Figs. 1 and 3) leads to an indeterminate equation for solving the LTM kernel. This is an indication of a missing state variable for describing the LTM dynamics. So here we postulate that the LTM dynamics is governed by both the time-varying amplitude and frequency of the input envelope, rather than the amplitude alone. Indeed the PA input signal $\hat{x}(t) = |\hat{x}(t)|e^{j\angle\hat{x}(t)}$ is composed of two independent variables, the amplitude and phase $(|\hat{x}(t)|, \angle\hat{x}(t))$, constituting the two basic state variables of the system. We then observe that the output of the LTM path $\hat{y}_{\rm LT}(t)$ in the structures Figs. 1–3 is actually a modulation coefficient of the input signal, or in other terms, it is a pattern of the system transfer function and not the system output signal. As such, we justify the above given postulate by the following:

a) as indicated previously, the transfer function of a time-invariant system is invariant to the input signal phase [24], [25], [1];
b) transfer function of a dynamic system is a function of input signal frequency, i.e., the derivative of input signal phase;
c) transfer function of a nonlinear system is a function of the input signal amplitude.

Accordingly, we enhance the model (5) to the following:

$$\hat{y}_{\rm ST}(t) = \int_0^\infty \hat{h}_{\rm ST}(|\hat{x}(t-\tau)|,\tau)\hat{x}(t-\tau)d\tau \tag{15.1}$$

$$\begin{aligned}
\hat{y}_{\rm LT}(t) = &\int_0^\infty \hat{h}_{\rm LT1}(|\hat{x}(t-\tau)|,\tau)|\hat{x}(t-\tau)|d\tau\\
&+ \int_0^\infty \hat{h}_{\rm LT2}(|\hat{x}(t-\tau)|,\tau)\omega_{\hat{x}}(t-\tau)d\tau
\end{aligned} \tag{15.2}$$

$$\hat{y}(t) = (1+\hat{y}_{\rm LT}(t))\hat{y}_{\rm ST}(t) \tag{15.3}$$

where we have defined the instantaneous phase and frequency of the envelope $\hat{x}(t)$ as

$$\begin{aligned}
\phi_{\hat{x}}(t) &= \tan^{-1}\left[-j\frac{\hat{x}(t)-\hat{x}(t)^*}{\hat{x}(t)+\hat{x}(t)^*}\right]\\
\omega_{\hat{x}}(t) &= \frac{d\phi_{\hat{x}}(t)}{dt}.
\end{aligned} \tag{15.4}$$

Note that in order to limit the model complexity we have assumed that the LTM modulation $\hat{y}_{\rm LT}(t)$ depends linearly on the time-varying frequency, while it is nonlinearly dependent on the amplitude. The assumption of linearity with respect to instantaneous frequency can be understood by the fact that, as illustrated in Fig. 2, if one drives the PA with a two-tone signal for example, the amplitude of the beat frequency component which is

the source of the LTM modulation depends strongly on the amplitude and spacing of the two tones, but only mildly on the value of the two frequencies (provided they remains reasonably within the bandwidth). Amplitude and spacing of the two tones are a projection of the envelope signal amplitude value $|\hat{x}(t)|$ and its time velocity, while the average value of two tone frequencies is a projection of envelope instantaneous frequency $\omega_{\hat{x}}(t)$. Moreover, for the sake of spectral resource preservation, the instantaneous frequency hop in communication signals is usually kept small compared to the carrier frequency. The model topology is now as illustrated in Fig. 5.

Observing as previously that $\hat{y}_{\rm LT}(t)$ in (15.2) is null for a single-tone CW input $\hat{x}(t) = \hat{X}_0 e^{j\Omega t}$ (both the amplitude $|\hat{x}(t)|$ and the frequency $\omega_{\hat{x}}(t)$ are time-invariant in this case), the identification of the STM kernel remains unchanged from Section III.

For the extraction of the two LTM kernels, we still apply the two-tone signal (12), from which we see that, provided $\hat{X}_0$ and $\hat{X}_1$ are real, the time-varying phase and frequency are expressed as follows:

$$\phi_{\hat{x}}(t) = \tan^{-1}\left(\frac{X_1 \sin(\Omega t)}{X_0 + X_1 \cos(\Omega t)}\right) \simeq \frac{X_1 \sin(\Omega t)}{X_0} \quad (16.1)$$

$$\omega_{\hat{x}}(t) = \frac{d\phi_{\hat{x}}(t)}{dt} = \frac{X_1}{X_0}\Omega \cos(\Omega t). \quad (16.2)$$

The new LTM time-varying frequency-domain kernels are defined

$$\hat{H}_{\rm LT1}(|\hat{x}(t)|, \omega) = \int_0^\infty \hat{h}_{\rm LT1}(|\hat{x}(t)|, \tau) e^{-j\omega\tau} d\tau$$

$$\hat{H}_{\rm LT2}(|\hat{x}(t)|, \omega) = \int_0^\infty \hat{h}_{\rm LT2}(|\hat{x}(t)|, \tau) e^{-j\omega\tau} d\tau. \quad (17)$$

Taking into account the new variable (16.2) and reconsidering accordingly the steps in Appendix I-A, with the now two LTM kernels, we readily find the well conditioned system of four equations in four unknowns below, for solving $\hat{H}_{\rm LT1}(\hat{X}_0, \pm\Omega)$ and $\hat{H}_{\rm LT2}(\hat{X}_0, \pm\Omega)$

$$2\frac{Y^+_{\rm LT}(\hat{X}_0, \Omega)}{\hat{X}_1} = \hat{H}_{\rm LT1}(\hat{X}_0, \Omega) + \hat{X}_0 \frac{\partial \hat{H}_{\rm LT1}(\hat{X}_0, \Omega)}{\partial \hat{X}_0} + \frac{\Omega}{\hat{X}_0}\hat{H}_{\rm LT2}(\hat{X}_0, \Omega)$$

$$2\frac{Y^-_{\rm LT}(\hat{X}_0, \Omega)}{\hat{X}_1} = \hat{H}_{\rm LT1}(\hat{X}_0, -\Omega) + \hat{X}_0 \frac{\partial \hat{H}_{\rm LT1}(\hat{X}_0, -\Omega)}{\partial \hat{X}_0} + \frac{\Omega}{\hat{X}_0}\hat{H}_{\rm LT2}(\hat{X}_0, -\Omega)$$

$$2\frac{Y^+_{\rm LT}(\hat{X}_0, -\Omega)}{\hat{X}_1} = \hat{H}_{\rm LT1}(\hat{X}_0, -\Omega) + \hat{X}_0 \frac{\partial \hat{H}_{\rm LT1}(\hat{X}_0, -\Omega)}{\partial \hat{X}_0} - \frac{\Omega}{\hat{X}_0}\hat{H}_{\rm LT2}(\hat{X}_0, -\Omega)$$

$$2\frac{Y^-_{\rm LT}(\hat{X}_0, -\Omega)}{\hat{X}_1} = \hat{H}_{\rm LT1}(\hat{X}_0, \Omega) + \hat{X}_0 \frac{\partial \hat{H}_{\rm LT1}(\hat{X}_0, \Omega)}{\partial \hat{X}_0} - \frac{\Omega}{\hat{X}_0}\hat{H}_{\rm LT2}(\hat{X}_0, \Omega). \quad (18)$$

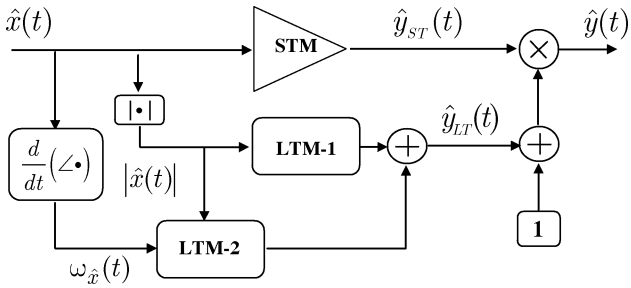

Fig. 5. Modified FF model topology.

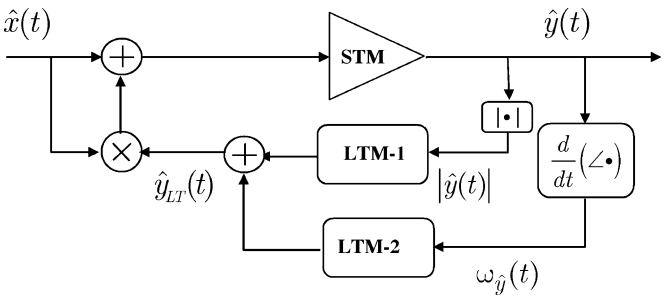

Fig. 6. New FB model topology.

As for the STM characterization, the input amplitude $\hat{X}_0$ and frequency Ω are to be swept throughout the operating input amplitude range and frequency bandwidth respectively, in order to fully characterize the PA LTM dynamics. The LTM extraction (18) is a differential equation system in the variable $\hat{X}_0$, that can be efficiently and accurately resolved as described in Appendix I-B.

V. FB Model Topology

As stated before, the FF topology considered in Section IV is a first-order truncation of the FB structure characterizing LTM mechanisms in the PA. The FF structure is conceivable when the long-term modulation of the quiescent point due to memory remains small or moderate, which is usually the case. Nevertheless for increased accuracy and more generality, it is of interest to investigate the FB topology. Though this topology has been indicated many times in the past for illustration purposes, a full identification of its characteristics has not been carried out so far.

We will show below that the methodology used to identify the characteristics of the FF topology can be readily extended to the FB topology.

First, we will reconsider the FB topology, Fig. 1, in order to account for the new state-variable (time-varying frequency) discussed above. The model topology is therefore as is illustrated in Fig. 6.

Considering the signals at the various model nodes, the PA is thus defined by the following equation:

$$\hat{y}(t) = \int_0^\infty \hat{h}_{\rm ST}(|[1 + \hat{y}_{\rm LT}(t-\tau)] \cdot \hat{x}(t-\tau))|, \tau) \cdot [1 + \hat{y}_{\rm LT}(t-\tau)] \cdot \hat{x}(t-\tau) d\tau \quad (19.1)$$

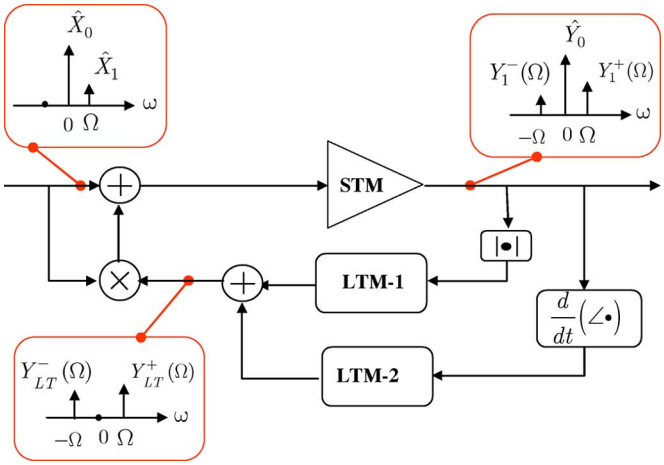

Fig. 7. FB LTM kernels extraction bench.

$$\hat{y}_{\rm LT}(t) = \int_0^\infty \hat{h}_{\rm LT1}(|\hat{x}(t-\tau)|,\tau)|\hat{y}(t-\tau)|d\tau + \int_0^\infty \hat{h}_{\rm LT2}(|\hat{x}(t-\tau)|,\tau)\omega_{\hat{y}}(t-\tau)d\tau. \quad (19.2)$$

We again observe that, as seen previously with the FF topology, the LTM term $\hat{y}_{\rm LT}(t)$ is null when the PA is driven with a single-tone CW signal $\hat{x}(t) = \hat{X}_0 e^{j\Omega t}$. Therefore, the STM kernel identification remains unchanged, i.e.,

$$\hat{H}_{\rm ST}(\hat{X}_0,\Omega) = \frac{\hat{y}(t)}{\hat{x}(t)} = \frac{\hat{Y}_0(\hat{X}_0,\Omega)}{\hat{X}_0}, \quad \hat{x}(t) = \hat{X}_0 e^{j\Omega t}. \quad (20)$$

For identifying the LTM kernels we again drive the PA with the two-tone stimulus (12). As in the illustration, Fig. 7, this will generate a three-tone signal at the PA output and a two-tone signal at the LTM block output node as follows:

$$\hat{y}(t) = \hat{Y}_0(\hat{X}_0,0) + \hat{Y}_1^+(\hat{X}_0,\Omega)e^{j\Omega_1 t} + \hat{Y}_1^-(\hat{X}_0,\Omega)e^{-j\Omega t} \quad (21.1)$$

$$\omega_{\hat{y}}(t) = \Omega\frac{\varphi_1(\hat{X}_0,\Omega)}{2}e^{j\Omega t} + \Omega\frac{\varphi_1^*(\hat{X}_0,\Omega)}{2}e^{-j\Omega t} \quad (21.2)$$

$$\hat{y}_{\rm LT}(t) = \hat{Y}_{\rm LT}^+(\hat{X}_0,\Omega)e^{j\Omega t} + \hat{Y}_{\rm LT}^-(\hat{X}_0,\Omega)e^{-j\Omega t}. \quad (21.3)$$

The components of $\hat{y}(t)$ and $\omega_{\hat{y}}(t)$ are directly acquired from the experiment; we have to identify the components of $\hat{y}_{\rm LT}(t)$ from (19). Thus, following the derivations in Appendix I-C, we find the following equation system from which these can be computed:

$$\begin{bmatrix} \hat{Y}_1^+(\hat{X}_0,\Omega) - c_{11}\hat{X}_1 \\ \hat{Y}_1^{-*}(\hat{X}_0,\Omega) - c_{21}\hat{X}_1 \end{bmatrix} = \begin{bmatrix} c_{11} & c_{12} \\ c_{21} & c_{22} \end{bmatrix} \begin{bmatrix} \hat{Y}_{\rm LT}^+(\hat{X}_0,\Omega) \\ \hat{Y}_{\rm LT}^{-*}(\hat{X}_0,\Omega) \end{bmatrix}$$

$$c_{11} = \hat{H}_{\rm ST}(\hat{X}_0,\Omega) + \frac{1}{2}\frac{\partial \hat{H}_{\rm ST}(\hat{X}_0,\Omega)}{\partial \hat{X}_0}\hat{X}_0$$

$$c_{12} = \frac{1}{2}\frac{\partial \hat{H}_{\rm ST}(\hat{X}_0,\Omega)}{\partial \hat{X}_0}\hat{X}_0$$

$$c_{21} = \frac{1}{2}\frac{\partial \hat{H}_{\rm ST}^*(\hat{X}_0,-\Omega)}{\partial \hat{X}_0}\hat{X}_0$$

$$c_{22} = \hat{H}_{\rm ST}^*(\hat{X}_0,-\Omega) + \frac{1}{2}\frac{\partial \hat{H}_{\rm ST}^*(\hat{X}_0,-\Omega)}{\partial \hat{X}_0}\hat{X}_0. \quad (22)$$

Finally, with the four components $\hat{Y}_{\rm LT}^+(\hat{X}_0,\pm\Omega)$ and $\hat{Y}_{\rm LT}^-(\hat{X}_0,\pm\Omega)$ determined we can use the differential equation (A3.4) in Appendix I-C, to solve the two LTM kernels $\hat{H}_{\rm LT1}(\hat{X}_0,\Omega)$ and $\hat{H}_{\rm LT2}(\hat{X}_0,\Omega)$.

VI. Model Numerical Implementation

The model (15) is a nonlinear convolution integral form that needs to be digitized efficiently in a computer implementation, from the knowledge of the 3 TVFD kernels $\hat{H}_{\rm ST}(|\hat{x}|,\Omega)$, $\hat{H}_{\rm LT1}(|\hat{x}|,\Omega)$ and $\hat{H}_{\rm LT2}(|\hat{x}|,\Omega)$. An efficient way to handle the problem is to use the orthogonal lookup-table decomposition method from Quindroit *et al.* [40] together with the vector fitting pole/residue approximation from Gustavsen [41]–[43]. We recall the approach briefly below; more details can be found in the indicated references. The principal idea is to project each 2-D kernel $\hat{H}(|\hat{x}|,\Omega)$ onto two single-dimensional basis $\langle\alpha_p(\Omega)\rangle$ and $\langle\beta_p(|\hat{x}|)\rangle$, so that

$$\hat{H}(|\hat{x}|,\Omega) = \sum_{p=1}^{P}\alpha_p(\Omega)\beta_p(|\hat{x}|). \quad (23)$$

The usual choice for basis functions $\beta_p(|\hat{x}|)$ is usually the monomial $|\hat{x}|^{2p}$ which is known to be ill-conditioned; in [40], we propose a better choice that is to construct an optimal orthogonal basis $\langle\beta_p(|\hat{x}|)\rangle$ using singular-value decomposition (SVD) and cubic-splines functions. Once the basis $\langle\beta_p(|\hat{x}|)\rangle$ is formed, the other basis $\langle\alpha_p(\Omega)\rangle$ is easily determined by least-square fitting.

Basis $\langle\alpha_p(\Omega)\rangle$ then represents a series of linear filters that can be effectively synthesized with the vector fitting method [41]–[43] guaranteeing the model integration stability, i.e.,

$$\alpha_p(\Omega) = \sum_{m=1}^{M}\frac{r_{p,m}}{j\Omega - \nu_{p,m}} \quad (24)$$

where all poles $\nu_{p,m}$ have negative real part.

Accounting for (23) and (24) in (15) or (19), each of the nonlinear convolution integral involved takes the following general form:

$$\hat{z}(t_n) = \int_0^\infty \hat{h}(|\hat{x}(t_n-\tau)|,\tau)\hat{x}(t_n-\tau)d\tau = \sum_{p=1}^{P}\sum_{m=1}^{M} r_{p,m}\int_0^{t_n} e^{\nu_{p,m}(t_n-\tau)}\beta_p(|\hat{x}(\tau)|)\hat{x}(\tau)d\tau. \quad (25)$$

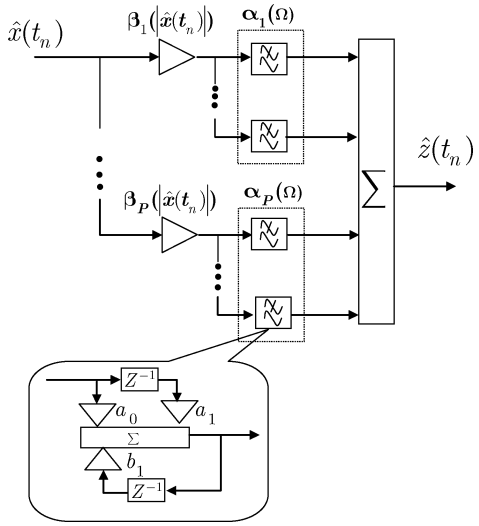

Fig. 8. Nonlinear-integral kernel implementation.

Digitizing the convolution integral in (25) using piece-wise linear approximation of inputs to filters finally yields the ultimate discrete form of the proposed model

$$\begin{aligned}\hat{z}(t_n) &= \sum_{p=1}^{P}\sum_{m=1}^{M} r_{p,m} w_{p,m}(t_n)\\ w_{p,m}(t_n) &= a_0\beta_p(|\hat{x}(t_n)|)\hat{x}(t_n) + a_1\beta_p(|\hat{x}(t_{n-1})|)\hat{x}(t_{n-1})\\ &\quad + b_1 w_{p,m}(t_{n-1})\\ a_0 &= (b_1 - \nu_{p,m}\Delta t_n - 1)/\nu_{p,m}^2\Delta t_n\\ a_1 &= -[b_1(1-\nu_{p,m}\Delta t_n) - 1]/\nu_{p,m}^2\Delta t_n\\ b_1 &= e^{\nu_{p,m}\Delta t_n}\\ \Delta t_n &= t_n - t_{n-1}. \end{aligned} \tag{26}$$

The model is thus implemented as a P-parallel filter bank (parallel Hammerstein structure), as illustrated in Fig. 8; each branch is composed of a nonlinear memoryless block driving a parallel connection of linear IIR filters. Each linear filter has only a single delay tap, with a delay value adjusted to the incoming signal speed to ensure accuracy. As for the characteristics $\langle\beta_p(|\hat{x}|)\rangle$ of the memoryless blocks, being orthogonal in construction, the number of branches P is optimally small, usually less than five. This shows that, compared to the explicit-discrete-time modeling approach, the continuous-time modeling approach is amenable in a more systematic and controllable way to an optimal discrete-time model implementation.

VII. Application Example

Both model extraction and implementation processes described in the previous sections are summarized in algorithmic forms in Appendix I-D and I-E respectively. These algorithms were realized in MATLAB. To verify the theory herein developed, we have considered the modeling a typical, one stage, narrow band, 14 dB gain, 25 dBm output RF MOS amplifier, working at 830 MHz center frequency, with 5% bandwidth. All the experiments were carried out from simulation, using Agilent-EEsof ADS/Ptolemy and MATLAB cosimulation. For the interested reader, the circuit schematic can be found in

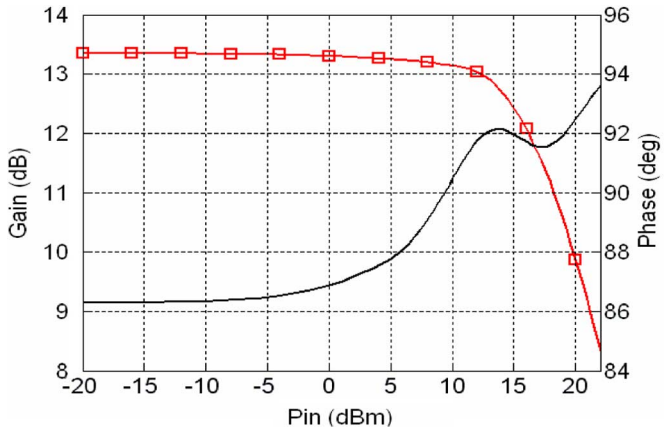

Fig. 9. PA gain and phase shift at center frequency (830 MHz).

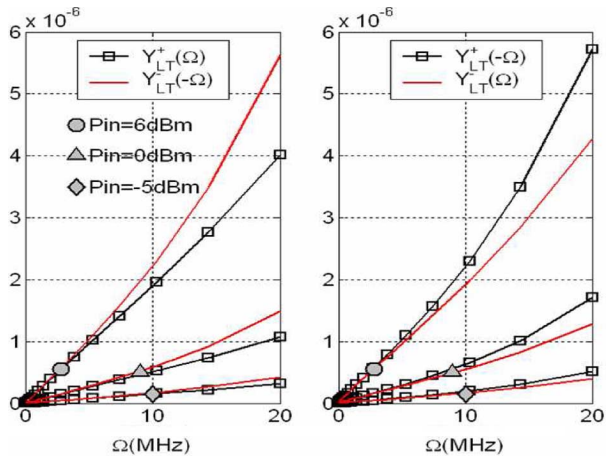

Fig. 10. FF model LTM output components.

Agilent-ADS amplifier example project [44]. This example has been chosen because it converges easily with both HB and Envelope analysis, so that it allows an effective comparison between the models and the circuit simulation for any type of stimulus.

Fig. 9 shows the gain compression and phase shift of the PA at center frequency.

From the extraction process (Appendix I-D, Section 2), Step 4), we have recorded the LTM path output components $Y^+_{\rm LT}(\hat{X}_0,\pm\Omega)$ and $Y^-_{\rm LT}(\hat{X}_0,\pm\Omega)$. Fig. 10 shows the plot of the four components, as a function of the frequency offset, for three levels of input amplitude $\hat{X}_0$. These are unitless components. We may see from the plots that the condition (14) is not verified here; $Y^+_{\rm LT}(\Omega)$ and $Y^-_{\rm LT}(-\Omega)$, as well as $Y^-_{\rm LT}(\Omega)$ and $Y^+_{\rm LT}(-\Omega)$ grow farther apart as the frequency offset increases. This confirms the need for a supplementary state variable in describing the LTM memory mechanisms, as we discussed in Sections III and IV.

For illustration purposes, Fig. 11 presents 3-D plots showing the shape of the three frequency-domain kernels for the FF model.

We have performed a classical third-order IMD test, with two identical large-signal tones, fixing one of the tones at bandwidth center and sweeping the other to either of the bandwidth ends.

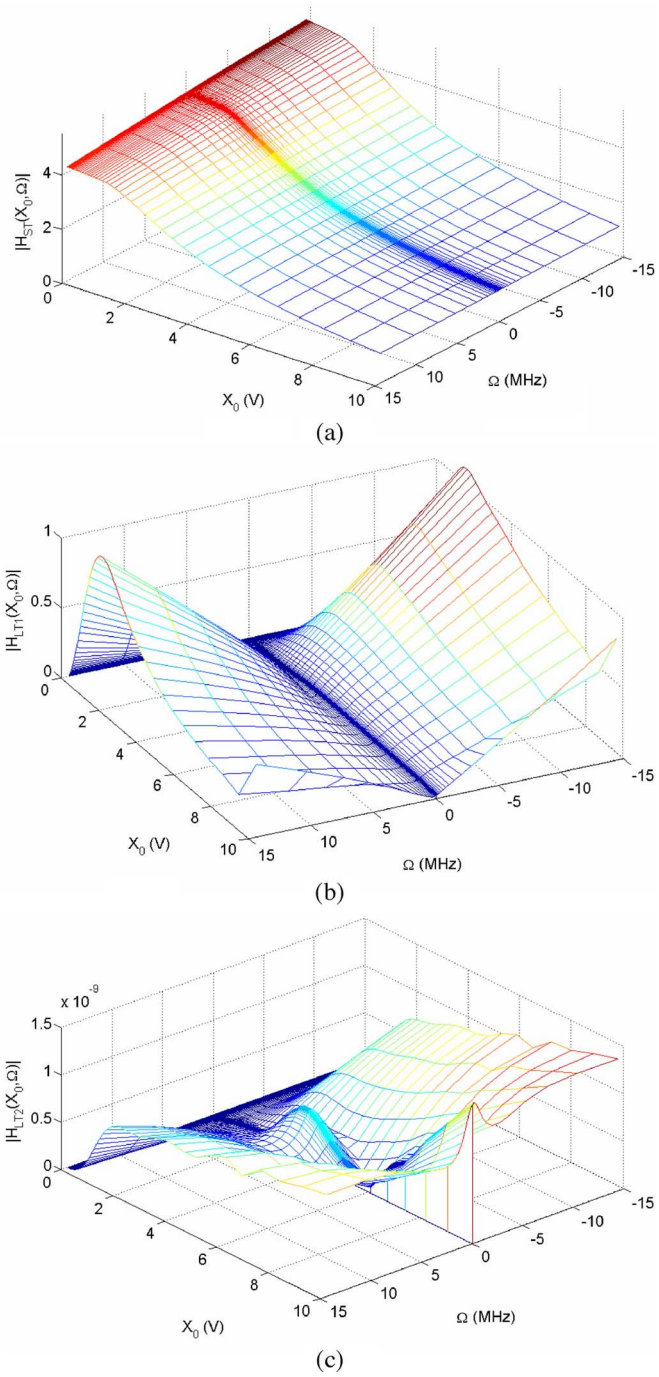

Fig. 11. Modified FF model kernels: (a) $\hat{H}_{\mathrm{ST}}(\hat{X}_0, \Omega)$; (b) $\hat{H}_{\mathrm{LT1}}(\hat{X}_0, \Omega)$; (c) $\hat{H}_{\mathrm{LT2}}(\hat{X}_0, \Omega)$.

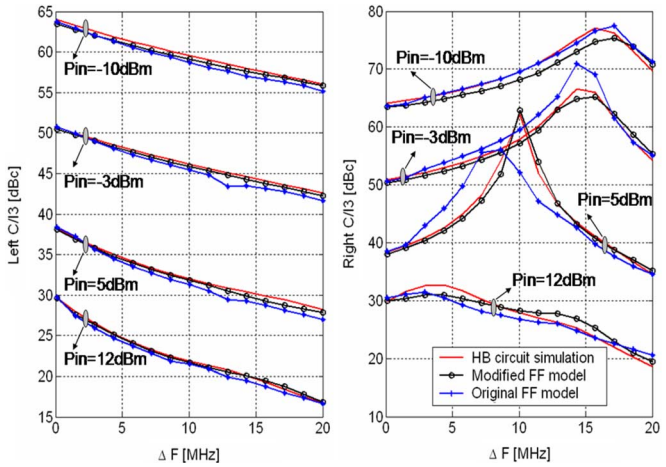

Fig. 12. Left and right IMD3 plots: Comparison between circuit simulation, modified FF model, and original FF model.

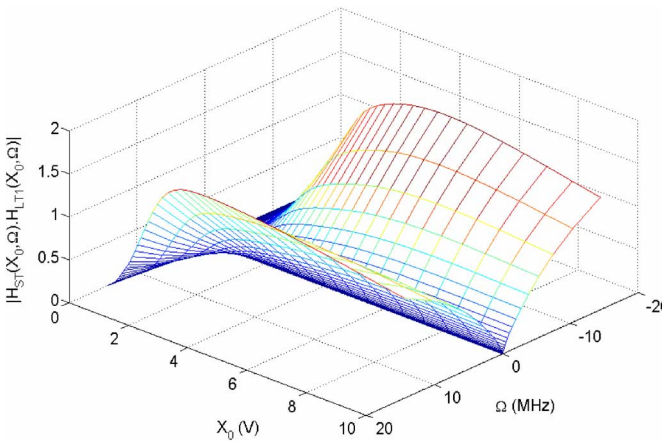

Fig. 13. FB model equivalent open-loop gain.

Fig. 12 shows the plot of the left and right hand IMD3, for four different input levels. The figure compares the HB circuit simulation with the original FF model and the modified FF model version. We may observe from the figure a number of important points: first, there are large asymmetries between right and left hand IMDs; second, there is an excellent match between the modified FF model version and HB simulation; third, the modified FF model provides a substantial improvement over the original version, especially in the IMD sweet spot regions.

The FB model version has also been extracted from the same data. In Fig. 13, we have plotted the product $\hat{H}_{\mathrm{ST}}(|\hat{X}_0|, \Omega) \times \hat{H}_{\mathrm{LT1}}(|\hat{X}_0|, \Omega)$ of the FB model; this product represents, in a sense, the open-loop gain of the FB model. We may see that the open-loop gain remains fairly small, inferring that a FF implementation would be a good approximate for the FB structure. As a result, we may see in Fig. 14 where we compare the IMD results from the FF and the FB model versions that they produce practically the same figures. We must say, however, that the FB model, precisely because of its FB structure, has a natural potential for instability, though we have not encountered such a situation here. The model being nonlinear, the stability conditions remains difficult to draw; hence in this context we prefer the FF model structure. In the next plots, for sake of figure readability, we will only show the FF model when necessary.

The second test stimulus considered is a pulse RF signal with a fixed carrier frequency 830 MHz. Fig. 15 shows the magnitude of the output pulse as a function of time, for four levels of input power. We see that the fit between the model and circuit simulation is good, even at high gain compression. Both the rising and falling edges are fairly well reproduced.

The third test stimulus we have considered is a more elaborate communication signal, a 3.84 MHz bandwidth WCDMA signal. With that signal we have carried out an ACPR analysis of the amplifier, with an input power sweep from the linear region up to 3 dB gain compression. Fig. 16 compares the left and

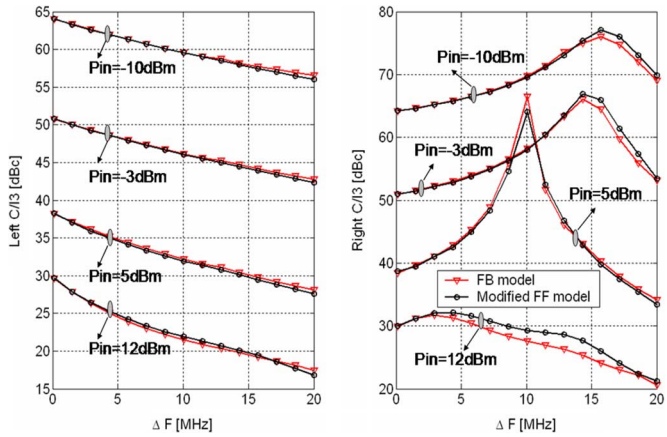

Fig. 14. IMD3 comparison between modified FF and FB model versions.

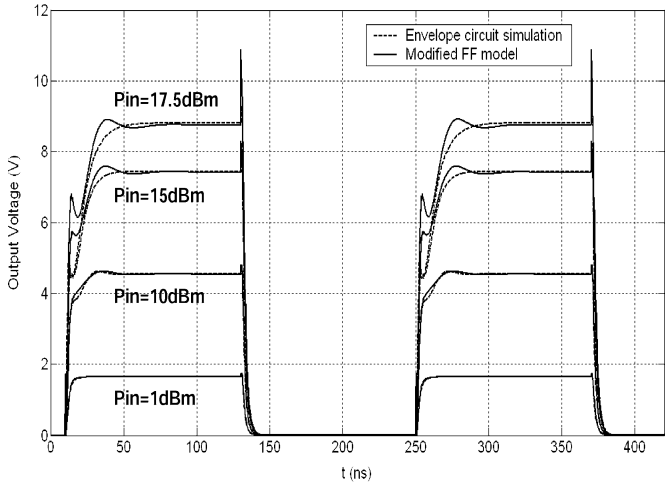

Fig. 15. RF pulse response: comparison between FF model and circuit simulation.

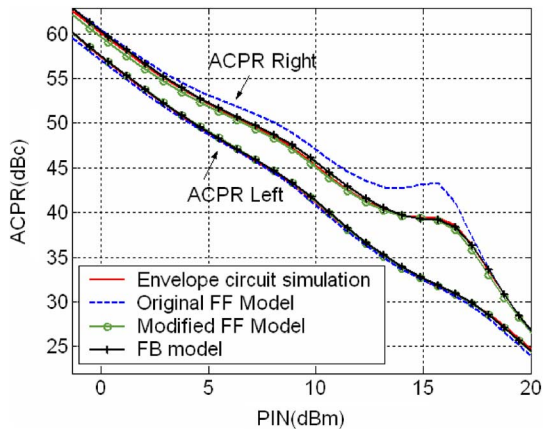

Fig. 16. Left and right ACPR plots: comparison between circuit simulation, original FF model, modified FF, and FB models.

right hand ACPR figures obtained from Envelope-transient circuit simulation, the original FF, the modified FF, and FB model versions. Again, we see important ACPR asymmetries and once again a close agreement of both the FF and the FB model with the circuit simulation. The improvement of the new models over the original FF model is also substantial, up to 5 dB. The model run time for the ACPR curve is a fraction of a minute, while it

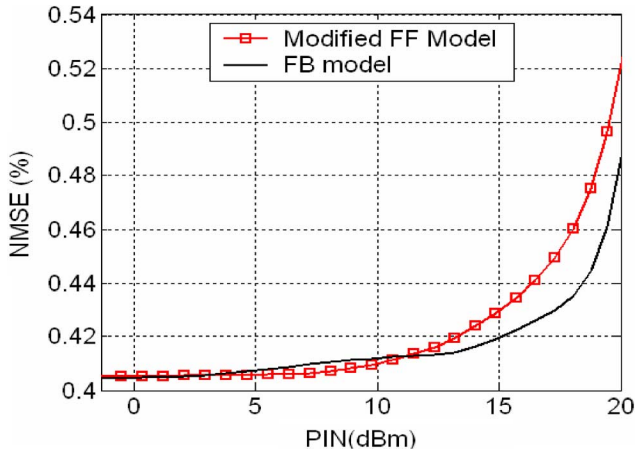

Fig. 17. NMSE (dB) for CDMA input signal.

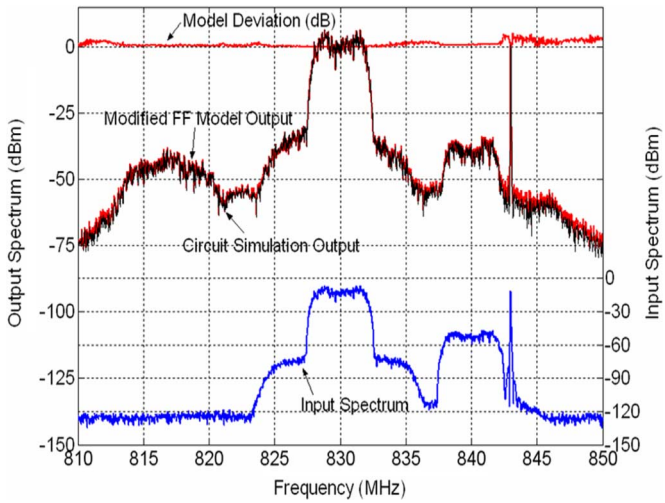

Fig. 18. Radio desensitization simulation—PA output spectrum: comparison between circuit simulation and FF model.

takes about two hours for the circuit simulation. Fig. 17 gives the plot of the normalized mean square error (NMSE) on the output waveform corresponding to the ACPR plot in Fig. 16, for both the FF and FB models. This remains less than 0.6% all over the input power range.

The last test we have carried out is a radio desensitization simulation. The amplifier is driven with a −40 dBm desired QAM16-OFDM RF channel, a −10 dBm CW interferer at 4 MHz offset and 10 dBm modulated interferer at 10 MHz offset. Fig. 18 shows the total spectra of the input and output signals. The model and circuit simulation results are superimposed on the figure. The decibel deviation between the two results is also shown in the figure. This is computed as the power spectral density difference between the model and the circuit simulation, at the same frequency. The NMSE of the model on the waveform is about 0.12%. There is again a close agreement of the model with the circuit simulation in this extremely complex and wideband stimulus configuration.

To conclude this application example, we can say that owing to the simplicity of the stimuli used to extract the model (CW large-signal tone + small-signal tone), and under the excellent performance of the model on large two-tone IMD analysis as

well as on pulsed RF signals and complex communication signals, the modeling approach proposed here effectively captures the fundamental invariants of the system making the model apply to arbitrary complex communication signals.

Unfortunately, we have not been able to complete the model extraction from the experimental setup; this is underway but it is currently hindered by the limitations of the available large-signal network analyzer equipment, especially phase calibration inaccuracies. We hope to complete this sometimes and show the results in a future communication. Nevertheless, the systematic PA modeling theory presented herein, validated on circuit simulation basis, is an invaluable advancement; especially for integrated systems design where discrete block hardware prototyping is not always an option. The model extracted from circuit schematic can then speedup the system-level verification. We expect that this article will find readers with the necessary equipments and good measurements expertise to test the extraction algorithm detailed in Appendix I-D.

VIII. Conclusion

This paper has presented a synthesis of past works on the continuous-time modeling principle, especially those addressing the nonlinear short-term and the long-term memory of the PA by means of the modified Volterra and nonlinear-integral approaches. It has clarified the concept of the two-memory-path model and provided the full theoretical details for the extraction of the model integral kernels and their effective numerical implementation. The so-called FF and FB model topologies have both been discussed; a singularity has been identified in model kernels extraction equation, and a new state variable is identified that resolves the issue.

The model is extracted from a simple stimulus (a large-signal CW tone and a small-signal tone) which guarantees an easy, fast, and accurate parameter extraction by HB simulation. The excellent model results obtained with large-signal two-tone stimuli as well as RF pulse and highly complex communication systems stimuli have validated the model topologies and extraction method. This now makes the PA modeling process stand in line with the well established transistor compact modeling process where the model parameters are extracted from simple dc and small-signal ac stimuli, and the model topology and extraction procedure validated on the response to large signal RF stimuli.

Despite the apparently cumbersome integral form of the model, this paper has shown how it lends itself to an optimal digital implementation, using well known and freely available numerical techniques.

Appendix

A. FF Model LTM Kernel Identification Equation

Given the input signal to the PA

$$\begin{aligned}&\hat{x}(t) = \hat{X}_0 + \hat{X}_1 e^{j\Omega t}\\ &\hat{X}_1 \ll 1\\ &\hat{X}_0, \hat{X}_1 \text{ real and positive}\end{aligned} \tag{A1.1}$$

we have

$$|\hat{x}(t)| = \sqrt{\hat{x}(t)\hat{x}(t)^*} \simeq \hat{X}_0 + \hat{X}_1 \cos(\Omega t). \tag{A1.2}$$

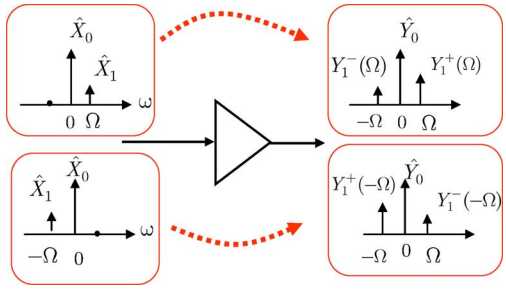

Fig. 19. Two-tone probe: left and right sideband stimulus.

Because $\hat{X}_1$ is small compared to unity, the output of the PA is a three-tone signal that we may note as in the following:

$$\hat{y}(t) = \hat{Y}_0(\hat{X}_0, 0) + \hat{Y}_1^+(\hat{X}_0, \Omega)e^{j\Omega t} + \hat{Y}_1^-(\hat{X}_0, \Omega)e^{-j\Omega t}. \tag{A1.3}$$

The components of the signal above are directly acquired from the amplifier output, either from measurements or HB simulation.

Inserting (A1.3) in the already identified STM path (5.1), and taking a first-order Taylor expansion we also find a three-tone signal as follows:

$$\begin{aligned}\hat{y}_{\mathrm{ST}}(t) &= \hat{Y}_0(\hat{X}_0, 0) + \hat{Y}_{\mathrm{ST}}^+(\hat{X}_0, \Omega)e^{j\Omega t}\\ &\quad + \hat{Y}_{\mathrm{ST}}^-(\hat{X}_0, \Omega)e^{-j\Omega t}\\ \hat{Y}_{\mathrm{ST}}^+(\hat{X}_0, \Omega) &= \left[\hat{H}_{\mathrm{ST}}(\hat{X}_0, \Omega) + \frac{1}{2}\frac{\partial \hat{H}_{\mathrm{ST}}(\hat{X}_0, \Omega)}{\partial \hat{X}_0}\hat{X}_0\right]\hat{X}_1\\ \hat{Y}_{\mathrm{ST}}^-(\hat{X}_0, \Omega) &= \frac{1}{2}\frac{\partial \hat{H}_{\mathrm{ST}}(\hat{X}_0, -\Omega)}{\partial \hat{X}_0}\hat{X}_0 \cdot \hat{X}_1.\end{aligned} \tag{A1.4}$$

Accounting of (A1.4) in (5.3), the output of the LTM path is found to be given by

$$\begin{aligned}\hat{y}_{\mathrm{LT}}(t) &= \hat{Y}_{\mathrm{LT}}^+(\hat{X}_0, \Omega)e^{j\Omega t} + \hat{Y}_{\mathrm{LT}}^-(\hat{X}_0, \Omega)e^{-j\Omega t}\\ \hat{Y}_{\mathrm{LT}}^+(\hat{X}_0, \Omega) &= \frac{\hat{Y}_1^+(\hat{X}_0, \Omega) - \hat{Y}_{\mathrm{ST}}^+(\hat{X}_0, \Omega)}{\hat{Y}_0(\hat{X}_0, 0)}\\ \hat{Y}_{\mathrm{LT}}^-(\hat{X}_0, \Omega) &= \frac{\hat{Y}_1^-(\hat{X}_0, \Omega) - \hat{Y}_{\mathrm{ST}}^-(\hat{X}_0, \Omega)}{\hat{Y}_0(\hat{X}_0, 0)}.\end{aligned} \tag{A1.5}$$

Note that the subscripts $+$ and $-$ in the above are used to designate respectively the synchronous and counter-synchronous output frequency components, as referred to the input component $\hat{X}_1 e^{j\Omega t}$; see illustration, Fig. 19.

Considering (A1.1)–(A1.2) in the expression of the LTM kernel, and taking a first-order Taylor expansion about $\hat{X}_0$ we have

$$\hat{h}_{\mathrm{LT}}(|\hat{x}(t)|, \tau) = \hat{h}_{\mathrm{LT}}(\hat{X}_0, \tau) + \hat{X}_1 \frac{\partial \hat{h}_{\mathrm{LT}}(\hat{X}_0, \tau)}{\partial \hat{X}_0}\cos(\Omega t). \tag{A1.6}$$

Thus, inserting (A1.6) in (5.2) and equating with (A1.5), we obtain the following differential equations system to be solved

for $\hat{H}_{\rm LT}(\hat{X}_0,\Omega)$ and $\hat{H}_{\rm LT}(\hat{X}_0,-\Omega)$, for all Ω between zero and half the PA bandwidth:

$$\begin{aligned}
\hat{H}_{\rm LT}(\hat{X}_0,0) &= 0\\
2\frac{Y^{+}_{\rm LT}(\hat{X}_0,\Omega)}{\hat{X}_1} &= \hat{H}_{\rm LT}(\hat{X}_0,\Omega)+\hat{X}_0\frac{\partial\hat{H}_{\rm LT}(\hat{X}_0,\Omega)}{\partial\hat{X}_0}\\
2\frac{Y^{-}_{\rm LT}(\hat{X}_0,\Omega)}{\hat{X}_1} &= \hat{H}_{\rm LT}(\hat{X}_0,-\Omega)+\hat{X}_0\frac{\partial\hat{H}_{\rm LT}(\hat{X}_0,-\Omega)}{\partial\hat{X}_0}\\
2\frac{Y^{+}_{\rm LT}(\hat{X}_0,-\Omega)}{\hat{X}_1} &= \hat{H}_{\rm LT}(\hat{X}_0,-\Omega)+\hat{X}_0\frac{\partial\hat{H}_{\rm LT}(\hat{X}_0,-\Omega)}{\partial\hat{X}_0}\\
2\frac{Y^{-}_{\rm LT}(\hat{X}_0,-\Omega)}{\hat{X}_1} &= \hat{H}_{\rm LT}(\hat{X}_0,\Omega)+\hat{X}_0\frac{\partial\hat{H}_{\rm LT}(\hat{X}_0,\Omega)}{\partial\hat{X}_0}\\
0\le\Omega\le\frac{Bw}{2},&\quad 0\le\hat{X}_0\le\hat{X}_{\max}. \qquad \text{(A1.7)}
\end{aligned}$$

B. Solution of the LTM Kernel-Identification Differential Equation

Given the differential equation (18) recalled below for convenience:

$$\begin{aligned}
&\hat{H}_{\rm LT1}(\hat{X}_0,\Omega)+\hat{X}_0\frac{\partial\hat{H}_{\rm LT1}(\hat{X}_0,\Omega)}{\partial\hat{X}_0}+\frac{\Omega}{\hat{X}_0}\hat{H}_{\rm LT2}(\hat{X}_0,\Omega)\\
&\quad=2\frac{Y^{+}_{\rm LT}(\hat{X}_0,\Omega)}{\hat{X}_1}\\
&\hat{H}_{\rm LT1}(\hat{X}_0,-\Omega)+\hat{X}_0\frac{\partial\hat{H}_{\rm LT1}(\hat{X}_0,-\Omega)}{\partial\hat{X}_0}+\frac{\Omega}{\hat{X}_0}\hat{H}_{\rm LT2}(\hat{X}_0,-\Omega)\\
&\quad=2\frac{Y^{-}_{\rm LT}(\hat{X}_0,\Omega)}{\hat{X}_1}\\
&\hat{H}_{\rm LT1}(\hat{X}_0,-\Omega)+\hat{X}_0\frac{\partial\hat{H}_{\rm LT1}(\hat{X}_0,-\Omega)}{\partial\hat{X}_0}-\frac{\Omega}{\hat{X}_0}\hat{H}_{\rm LT2}(\hat{X}_0,-\Omega)\\
&\quad=2\frac{Y^{+}_{\rm LT}(\hat{X}_0,-\Omega)}{\hat{X}_1}\\
&\hat{H}_{\rm LT1}(\hat{X}_0,\Omega)+\hat{X}_0\frac{\partial\hat{H}_{\rm LT1}(\hat{X}_0,\Omega)}{\partial\hat{X}_0}-\frac{\Omega}{\hat{X}_0}\hat{H}_{\rm LT2}(\hat{X}_0,\Omega)\\
&\quad=2\frac{Y^{-}_{\rm LT}(\hat{X}_0,-\Omega)}{\hat{X}_1}. \qquad \text{(A2.1)}
\end{aligned}$$

For a fixed offset frequency Ω, the differential equation can be resolved using classical Euler or trapezoidal rule, starting from $\hat{X}_0=0$ to $\hat{X}_0=\hat{X}_{\max}$, in order to determine the four terms $\hat{H}_{\rm LT1}(\hat{X}_0,\pm\Omega)$ and $\hat{H}_{\rm LT2}(\hat{X}_0,\pm\Omega)$.

This however requires fine steps of $\hat{X}_0$ in order to minimize the numerical integration error and ensure good extraction accuracy. On the other hand, since the kernels tend to be smooth functions of $\hat{X}_0$, a simpler and more accurate alternative is to consider a power expansion of the left and right side members of the equation, and equate the coefficients of the same power order. To that end we write

$$\begin{aligned}
\hat{H}_{\rm LT1}(\hat{X}_0,\Omega)&=\sum_{k=1}^{N}a_{1k}(\Omega)\hat{X}_0^k\\
\hat{H}_{\rm LT2}(\hat{X}_0,\Omega)&=\sum_{k=1}^{N}a_{2k}(\Omega)\hat{X}_0^{k+1}\\
Y^{+}_{\rm LT}(\hat{X}_0,\Omega)&=2\hat{X}_1\sum_{k=1}^{N}b_{1k}(\Omega)\hat{X}_0^k\\
Y^{-}_{\rm LT}(\hat{X}_0,\Omega)&=2\hat{X}_1\sum_{k=1}^{N}b_{2k}(\Omega)\hat{X}_0^k. \qquad \text{(A2.2)}
\end{aligned}$$

Note that the expansion has no power coefficient of order less than one for $\hat{H}_{\rm LT1}()$ and less than two for $\hat{H}_{\rm LT2}()$; this is so because LTM effects cannot be generated under small-signal excitation conditions. Inserting the expansion in the differential equation (18) and equating the coefficients of the same order, we readily obtain a simple algebraic equation from which we extract

$$\begin{aligned}
a_{1k}(\Omega)&=\frac{b_{1k}(\Omega)+b_{2k}(-\Omega)}{2(1+k)},\\
a_{2k}(\Omega)&=\frac{b_{1k}(\Omega)-b_{2k}(-\Omega)}{2\Omega}\\
a_{1k}(-\Omega)&=\frac{b_{2k}(\Omega)+b_{1k}(-\Omega)}{2(1+k)},\\
a_{2k}(-\Omega)&=\frac{b_{2k}(\Omega)-b_{1k}(-\Omega))}{2\Omega},\quad k=1,\ldots,N. \qquad \text{(A2.3)}
\end{aligned}$$

Then, for each pair of frequency offsets $\pm\Omega$, it suffices to compute the polynomial approximation of the four LTM path components, $Y^{+}_{\rm LT}(\hat{X}_0,\pm\Omega), Y^{-}_{\rm LT}(\hat{X}_0,\pm\Omega)$, obtained from (A1.5), and use (A2.3) to get the power expansion coefficients of the LTM kernels. Finally, we may then compose the kernels $\hat{H}_{\rm LT1}(\cdot)$ and $\hat{H}_{\rm LT2}(\cdot)$ using (A2.2) for any desired grid of $\hat{X}_0$.

C. Computing the Feedback LTM Kernels

Given the expression of $\hat{x}(t)$ in (12) and that of $\hat{y}_{\rm LT}(t)$ in (19.2) and inserting these in the STM path (19.1), we find

$$\begin{aligned}
\hat{y}(t)&=\int_0^{\infty}\hat{h}_{\rm ST}(w(t-\tau),\tau)\cdot z(t-\tau)d\tau\\
\hat{w}(t)&=\hat{X}_0+\hat{W}_1e^{j\Omega t}+\hat{W}_1^{*}e^{-j\Omega t}\\
\hat{W}_1&=\frac{1}{2}(\hat{X}_1+Y^{+}_{\rm LT}(\hat{X}_0,\Omega)+Y^{-*}_{\rm LT}(\hat{X}_0,\Omega))\\
z(t)&=\hat{X}_0+(\hat{X}_1+Y^{+}_{\rm LT}(\hat{X}_0,\Omega))e^{j\Omega t}+Y^{-}_{\rm LT}(\hat{X}_0,\Omega)e^{-j\Omega t}. \qquad \text{(A3.1)}
\end{aligned}$$

Carrying out a first-order expansion of $\hat{h}_{\rm ST}(|\hat{w}(t-\tau)|,\tau)$ around $\hat{X}_0$, we readily find that $\hat{y}(t)$ writes

$$\begin{aligned}
\hat{y}(t)&=\hat{H}_{\rm ST}(\hat{X}_0,\Omega)\hat{X}_0\\
&\quad+(c_{11}[\hat{X}_1+Y^{+}_{\rm LT}(\hat{X}_0,\Omega)]+c_{12}Y^{-*}_{\rm LT}(\hat{X}_0,\Omega))e^{j\Omega t}\\
&\quad+(c_{21}^{*}[\hat{X}_1^{*}+Y^{+*}_{\rm LT}(\hat{X}_0,\Omega)]+c_{22}^{*}Y^{-}_{\rm LT}(\hat{X}_0,\Omega))e^{-j\Omega t}\\
c_{11}&=\hat{H}_{\rm ST}(\hat{X}_0,\Omega)+\frac{1}{2}\frac{\partial\hat{H}_{\rm ST}(\hat{X}_0,\Omega)}{\partial\hat{X}_0}\hat{X}_0\\
c_{12}&=\frac{1}{2}\frac{\partial\hat{H}_{\rm ST}(\hat{X}_0,\Omega)}{\partial\hat{X}_0}\hat{X}_0\\
c_{21}&=\frac{1}{2}\frac{\partial\hat{H}^{*}_{\rm ST}(\hat{X}_0,-\Omega)}{\partial\hat{X}_0}\hat{X}_0\\
c_{22}&=\hat{H}^{*}_{\rm ST}(\hat{X}_0,-\Omega)+\frac{1}{2}\frac{\partial\hat{H}^{*}_{\rm ST}(\hat{X}_0,-\Omega)}{\partial\hat{X}_0}\hat{X}_0. \qquad \text{(A3.2)}
\end{aligned}$$

Equating (A3.2) with (21.1), we find the following algebraic equation for de-embedding the LTM components:

$$\begin{bmatrix} c_{11} & c_{12} \\ c_{21} & c_{22} \end{bmatrix} \begin{bmatrix} \hat{Y}_{\mathrm{LT}}^{+}(\hat{X}_0,\Omega) \\ \hat{Y}_{\mathrm{LT}}^{-*}(\hat{X}_0,\Omega) \end{bmatrix} = \begin{bmatrix} \hat{Y}_1^{+}(\hat{X}_0,\Omega) - c_{11}\hat{X}_1 \\ \hat{Y}_1^{-*}(\hat{X}_0,\Omega) - c_{21}\hat{X}_1 \end{bmatrix}. \tag{A3.3}$$

Finally once the four components $\hat{Y}_{\mathrm{LT}}^{+}(\hat{X}_0,\pm\Omega)$ and $\hat{Y}_{\mathrm{LT}}^{-}(\hat{X}_0,\pm\Omega)$ are determined, then similarly to the derivations in Appendix I-A, inserting (21.1) and (21.2) in (19.2) and considering a first-order expansion in $\hat{x}(t)$ around $\hat{X}_0$, we find the system below for solving the two LTM kernels $\hat{H}_{\mathrm{LT1}}(\hat{X}_0,\Omega)$ and $\hat{H}_{\mathrm{LT2}}(\hat{X}_0,\Omega)$

$$\begin{aligned}
2\frac{Y_{\mathrm{LT}}^{+}(\hat{X}_0,\Omega)}{\hat{X}_1} &= G_1(\hat{X}_0,\Omega)\cdot\hat{H}_{\mathrm{LT1}}(\hat{X}_0,\Omega) \\
&\quad + |\hat{Y}_0|\frac{\partial\hat{H}_{\mathrm{LT1}}(\hat{X}_0,\Omega)}{\partial\hat{X}_0} \\
&\quad + \Omega G_2(\hat{X}_0,\Omega)\hat{H}_{\mathrm{LT2}}(\hat{X}_0,\Omega) \\
2\frac{Y_{\mathrm{LT}}^{-}(\hat{X}_0,\Omega)}{\hat{X}_1} &= G_1^{*}(\hat{X}_0,\Omega)\cdot\hat{H}_{\mathrm{LT1}}(\hat{X}_0,-\Omega) \\
&\quad + |\hat{Y}_0|\frac{\partial\hat{H}_{\mathrm{LT1}}(\hat{X}_0,-\Omega)}{\partial\hat{X}_0} \\
&\quad + \Omega G_2^{*}(\hat{X}_0,\Omega)\cdot\hat{H}_{\mathrm{LT2}}(\hat{X}_0,-\Omega) \\
\frac{1}{2}\frac{Y_{\mathrm{LT}}^{+}(\hat{X}_0,-\Omega)}{\hat{X}_1} &= G_1(\hat{X}_0,-\Omega)\cdot\hat{H}_{\mathrm{LT1}}(\hat{X}_0,-\Omega) \\
&\quad + |\hat{Y}_0|\frac{\partial\hat{H}_{\mathrm{LT1}}(\hat{X}_0,-\Omega)}{\partial\hat{X}_0} \\
&\quad - \Omega G_2(\hat{X}_0,-\Omega)\cdot\hat{H}_{\mathrm{LT2}}(\hat{X}_0,-\Omega) \\
\frac{1}{2}\frac{Y_{\mathrm{LT}}^{-}(\hat{X}_0,-\Omega)}{\hat{X}_1} &= G_1(\hat{X}_0,-\Omega)\cdot\hat{H}_{\mathrm{LT1}}(\hat{X}_0,\Omega) \\
&\quad + |\hat{Y}_0|\frac{\partial\hat{H}_{\mathrm{LT1}}(\hat{X}_0,\Omega)}{\partial\hat{X}_0} \\
&\quad - \Omega G_2^{*}(\hat{X}_0,-\Omega)\cdot\hat{H}_{\mathrm{LT2}}(\hat{X}_0,\Omega)
\end{aligned} \tag{A3-3}$$

where from (21) we have set

$$\begin{aligned}
G_1(\hat{X}_0,\Omega) &= \left(\frac{Y_1^{+}(\hat{X}_0,\Omega)}{\hat{Y}_0} + \frac{Y_1^{-*}(\hat{X}_0,\Omega)}{\hat{Y}_0^{*}}\right)\cdot\frac{|\hat{Y}_0|}{\hat{X}_1} \\
G_2(\hat{X}_0,\Omega) &= \frac{\phi_1(\hat{X}_0,\Omega)}{\hat{X}_1} \\
\hat{Y}_0 &= \hat{Y}_0(\hat{X}_0,0).
\end{aligned}$$

D. Model Kernels Extraction Algorithm

Two variants of the TMP model have been described in this paper, namely the FF and the FB models. They are composed each of a STM and two LTM kernels. The models differ only on the LTM kernels; the STM kernel is identical for both.

Let Bw be the amplifier bandwidth and ω_0 be the center frequency. Consider a discrete set of $2K+1$ frequency points

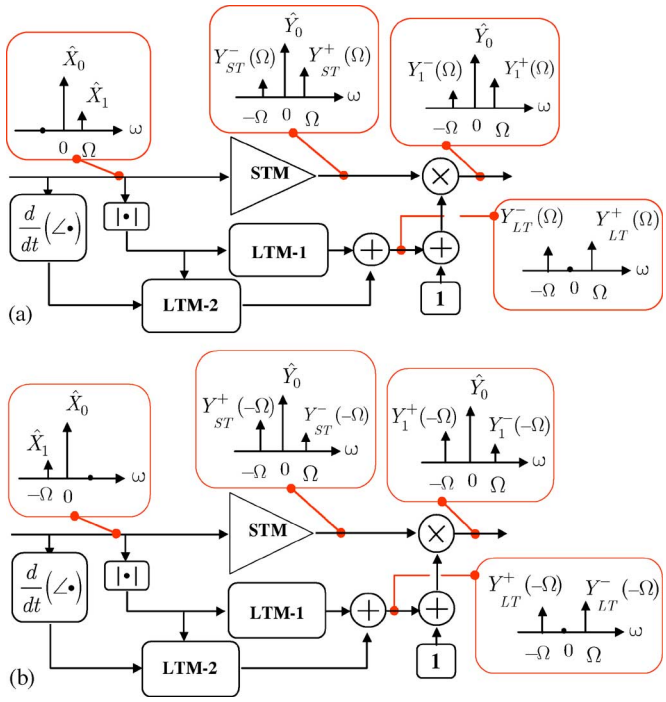

Fig. 20. FF LTM kernels identification measurement bench: (a) right sideband stimulus and (b) left sideband stimulus.

$\omega_0-\Delta\omega_K,\ldots,\omega_0-\Delta\omega_1,\omega_0,\omega_0+\Delta\omega_1,\ldots,\omega_0+\Delta\omega_K$ covering the bandwidth. The extraction process of the kernels can then be summarized in an algorithmic form as follows.

1) STM Kernel Extraction: For each frequency offset Ω in the set $\{-\Delta\omega_K,\ldots,-\Delta\omega_1,0,\Delta\omega_1,\ldots,\Delta\omega_K\}$, do the following.

Step 1) Drive the amplifier with a CW stimulus $x(t) = \Re e(\hat{X}_0\cdot e^{j(\omega_0+\Omega)t})$ and acquire the output signal $y(t) = \Re e(\hat{Y}(|\hat{X}_0|,\Omega)\cdot e^{j(\omega_0+\Omega)t})$.

Step 2) Form the STM kernel as the ratio of the output to the input complex amplitude: $\hat{H}_{\mathrm{ST}}(|\hat{X}_0|,\Omega) = \hat{Y}_0(|\hat{X}_0|,\Omega)/\hat{X}_0$.

Step 3) Repeat Steps 1)–2) for varying input amplitude $|\hat{X}_0|$, typically from linear region to 5 dB gain compression. A number of 30 amplitude points is usually sufficient.

2) LTM Kernel Extraction for FF Model: The FF LTM kernels extraction follows the measurement bench illustrated Fig. 20. It uses two stimulus configurations, a right sideband and a left sideband stimulus. This is summarized below.

For each frequency offset Ω in the positive half set $\{0,\Delta\omega_1,\ldots,\Delta\omega_K\}$, do the following.

Step 1) Drive the amplifier with a two-tone right sideband stimulus $x(t) = \Re e(\hat{X}_0\cdot e^{j\omega_0 t} + \hat{X}_1\cdot e^{j(\omega_0+\Omega)t})$, with the small-signal component $\hat{X}_1$ at least 30 dB below the large component $\hat{X}_0$, and acquire the three-tone output signal

$$\begin{aligned}
y(t) = \Re e\Big(&\hat{Y}_0(|\hat{X}_0|,0)e^{j\omega_0 t} \\
&+\hat{Y}_1^{+}(|\hat{X}_0|,\Omega)e^{j(\omega_0+\Omega)t} + \hat{Y}_1^{-}(|\hat{X}_0|,\Omega)e^{j(\omega_0-\Omega)t}\Big).
\end{aligned}$$

Then drive the amplifier with the left sideband stimulus $\bar{x}(t) = \Re e(\hat{X}_0 \cdot e^{j\omega_0 t} + \hat{X}_1 \cdot e^{j(\omega_0-\Omega)t})$ and acquire the corresponding output signal

$$\bar{y}(t) = \Re e\left(\hat{Y}_0(|\hat{X}_0|,0)e^{j\omega_0 t} + \hat{Y}_1^{+}(|\hat{X}_0|,-\Omega) \times e^{j(\omega_0-\Omega)t} + \hat{Y}_1^{-}(|\hat{X}_0|,-\Omega)e^{j(\omega_0+\Omega)t}\right).$$

When doing extraction from HB simulation, use a sufficiently large number of harmonics in the gain compression zone (higher than 10), and prefer the small-signal mixer mode; it provides the highest accuracy and simulation speed.

Step 2) Repeat Step 1 for varying input amplitude $|\hat{X}_0|$, typically from linear region to 5 dB gain compression. Record the four terms (small-signal response and the third-order IMD terms) $\hat{Y}_1^{+}(|\hat{X}_0|,\pm\Omega)$ and $\hat{Y}_1^{-}(|\hat{X}_0|,\pm\Omega)$ as a function of $|\hat{X}_0|$.

Step 3) Apply the same input stimulus (Steps 1)–2) to the STM kernel previously extracted to obtain the small-signal response and the third-order IMD terms generated by the STM path: $\hat{Y}_{\mathrm{ST}}^{+}(|\hat{X}_0|,\pm\Omega)$ and $\hat{Y}_{\mathrm{ST}}^{-}(|\hat{X}_0|,\pm\Omega)$, use (A1.4).

Step 4) Use (A1.5) to compute the four terms generated by the LTM path: $\hat{Y}_{\mathrm{LT}}^{+}(|\hat{X}_0|,\pm\Omega)$ and $\hat{Y}_{\mathrm{LT}}^{-}(|\hat{X}_0|,\pm\Omega)$.

Step 5) Use the polynomial method presented in Appendix I-B to solve the differential equation (18) describing the dynamics of the LTM kernels. More precisely, compute a polynomial approximation in $|\hat{X}_0|$ of the four measured characteristics $\hat{Y}_{\mathrm{LT}}^{+}(|\hat{X}_0|,\pm\Omega)$ and $\hat{Y}_{\mathrm{LT}}^{-}(|\hat{X}_0|,\pm\Omega)$. Then, with (A2.3), calculate the coefficients for the polynomial approximation of the LTM kernels $\hat{H}_{\mathrm{LT1}}(|\hat{X}_0|,\pm\Omega)$ and $\hat{H}_{\mathrm{LT2}}(|\hat{X}_0|,\pm\Omega)$ as a function of $|\hat{X}_0|$.

3) LTM Kernel Extraction for FB Model: The FB LTM kernel extraction follows the measurement bench illustrated Fig. 21; it is similar to the FF extraction bench, to the exception of a few details summarized below.

For each frequency offset Ω in the positive half set $\{0, \Delta\omega_1, \ldots, \Delta\omega_K\}$, do the following.

Step **s 1)–3)** IDEM FF LTM extraction.

Step **4)** Use (22) to compute the four terms generated by the LTM path: $\hat{Y}_{\mathrm{LT}}^{+}(|\hat{X}_0|,\pm\Omega)$ and $\hat{Y}_{\mathrm{LT}}^{-}(|\hat{X}_0|,\pm\Omega)$.

Step 5) The dynamics of the LTM kernels for the fixed pair of frequency offsets $\pm\Omega$ is described by the differential equation (A3.4). Equation (A3.4) cannot be solved as previously with a simple polynomial method, instead use the trapezoidal or Gear rule to integrate the differential equation from $|\hat{X}_0| = 0$ to the maximum value. The initial condition ($|\hat{X}_0| = 0$) for both $\hat{H}_{\mathrm{LT1}}(|\hat{X}_0|,\pm\Omega)$, and $\hat{H}_{\mathrm{LT2}}(|\hat{X}_0|,\pm\Omega)$ is zero since by definition, the LTM mechanism dies away in small signal conditions.

E. Model Implementation Algorithm

The two models presented herein are all composed of three TVFD kernels $\hat{H}_{\mathrm{ST}}(|\hat{x}|,\Omega)$, $\hat{H}_{\mathrm{LT1}}(|\hat{x}|,\Omega)$ and $\hat{H}_{\mathrm{LT2}}(|\hat{x}|,\Omega)$. The numerical implementation of each kernel is based on the orthogonal lookup table method summarized in algorithmic form as follows.

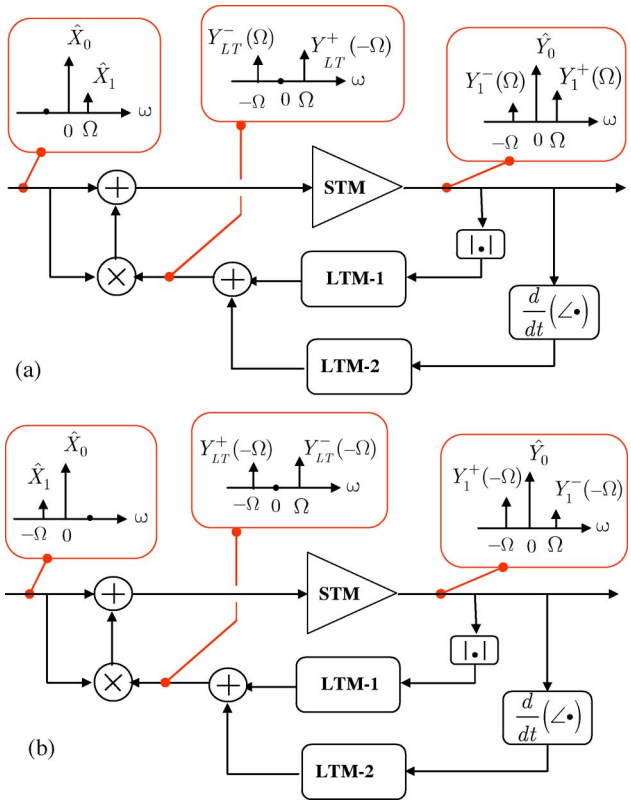

Fig. 21. Feedback LTM kernels identification measurement bench: (a) right sideband stimulus and (b) left sideband stimulus.

Step 1) Given a 2-D kernel $\hat{H}(|\hat{x}|,\Omega)$ extracted on discrete M input signal voltage points $|\hat{x}_1|, |\hat{x}_1|, \ldots, |\hat{x}_M|$ and N frequency offset points $|\Omega_1|, |\Omega_1|, \ldots, |\Omega_N|$, with $M \geq N$; form the $M \times N$ matrix $\boldsymbol{H} = [h_{ij}]$ such that $h_{ij} = \hat{H}(|\hat{x}_i|, \Omega_j)$.

Step 2) Use SVD algorithm to factor matrix $\boldsymbol{H}$ as $\boldsymbol{H} = \boldsymbol{U}\boldsymbol{S}\boldsymbol{V}^T$, where $\boldsymbol{S}$ is a diagonal matrix containing the singular values $s_1, s_2, \ldots, s_N$.
Consider only the P columns of the $M \times N$ matrix U corresponding to the most significant singular values, in order to form the $M \times P$ matrix $\boldsymbol{B} = [b_{ij}]$. A good threshold is $s_j / \max(s) \geq 1\mathrm{E}-5$.

Step 3) Use least square approximation to obtain the coefficients of the $P \times M$ matrix $\boldsymbol{A} = [a_{ij}]$ such that $\boldsymbol{B} \cdot \boldsymbol{A} = \boldsymbol{H}$.

Step 4) Each column of matrix $\boldsymbol{B}$ is a sampled version of a basis function over the input voltage $|\hat{x}|$; apply cubic spline interpolation on each column of $\boldsymbol{B}$ to construct the P continuous memoryless characteristics $\beta_p(|\hat{x}|)$ of the parallel Hammerstein structure, Fig. 8.
Each line of matrix $\boldsymbol{A}$ is a sampled version of a basis function over the frequency offset Ω; apply vector-fitting algorithm on each line of $\boldsymbol{A}$ to synthesize the P linear filters $\alpha_p(\Omega)$ in the Hammerstein structure, Fig. 8.

Note that SVD, cubic splines as well as vector-fitting methods are all freely available within MATLAB.

ACKNOWLEDGMENT

The authors would like to thank DGA/CELAR and also thank P. Le-Helleye for their support in this work.

REFERENCES

[1] J. Wood and D. Root, *Editors Fundamentals of Nonlinear Behavioral Modeling for RF and Microwave Design*. Boston, MA: Artech, 2005.

[2] J. C. Pedro and S. Maas, "A comparative overview of microwave and wireless power-amplifier behavioral modeling approaches," *IEEE Trans. Microw. Theory Tech.*, vol. 53, no. 4, pp. 1150–1163, Apr. 2005.

[3] W. Bosch and G. Gatti, "Measurement and simulation of memory effects in predistortion linearizers," *IEEE Trans. Microw. Theory Tech.*, vol. 37, no. 12, pp. 1885–1890, Dec. 1989.

[4] A. Carini, E. Mumolo, and G. Sicuranza, "V-vector algebra and its application to Volterra-adaptive filtering," *IEEE Trans. Circuits Syst. II, Analog Digit. Signal Process.*, vol. CAS2-46, no. 5, pp. 585–598, May 1999.

[5] Y. W. Fang, L. C. Jiao, X. D. Zhang, and J. Pan, "On the convergence of Volterra filter equalizers using a pth-order inverse approach," *IEEE Trans. Signal Process.*, vol. 49, no. 8, pp. 1734–1744, Aug. 2001.

[6] T. Wang and T. J. Brazil, "Volterra-mapping-based behavioral modeling of nonlinear circuits and systems for high frequencies," *IEEE Trans. Microw. Theory Tech.*, vol. 51, no. 5, pp. 1433–1440, May 2003.

[7] A. Zhu, P. J. Draxler, J. J. Yan, T. J. Brazil, D. F. Kimball, and P. M. Asbeck, "Open-loop digital predistorter for RF power amplifiers using dynamic deviation reduction-based Volterra series," *IEEE Trans. Microw. Theory Tech.*, vol. 56, no. 7, pp. 1524–1534, Jul. 2008.

[8] H. Ku and J. Kenney, "Behavioral modeling of nonlinear RF power amplifiers considering memory effects," *IEEE Trans. Microw. Theory Tech.*, vol. 51, no. 12, pp. 2495–2503, Dec. 2003.

[9] L. Ding, G. T. Zhou, D. R. Morgan, Z. Ma, J. S. Kenney, J. Kim, and C. R. Giardina, "A robust digital baseband predistorter constructed using memory polynomials," *IEEE Trans. Commun.*, vol. 52, no. 1, pp. 159–164, Jan. 2004.

[10] A. Ahmed, S. M. Endalkachew, and G. Kompa, "Power amplifier linearization using memory polynomial predistorter with non-uniform delay taps," in *IEEE MTT-S Int. Microw. Symp. Dig.*, Jun. 2004, vol. 3, pp. 1871–1874.

[11] H. Li, Z. Chen, and D. Wang, "Nonlinear least squares lattice algorithm for identifying the power amplifier with memory effects," in *Proc. IEEE Veh. Technol. Conf.*, 2006, pp. 2149–2153.

[12] W. J. Kim, K. J. Cho, S. P. Stapleton, and J. H. Kim, "Piecewise pre-equalized linearization of the wireless transmitter with a Doherty amplifier," *IEEE Trans. Microw. Theory Tech.*, vol. 54, no. 9, pp. 3469–3478, Sep. 2006.

[13] D. R. Morgan, Z. Ma, J. Kim, M. G. Zierdt, and J. Pastalan, "A generalized memory polynomial model for digital predistortion of RF power amplifiers," *IEEE Trans. Signal Process.*, vol. 54, no. 10, pp. 3852–3860, Oct. 2006.

[14] M. Ibnkahla, N. J. Bershad, J. Sombrin, and F. Castanié, "Neural network modeling and identification of nonlinear channels with memory: Algorithms, applications, and analytic models," *IEEE Trans. Signal Process.*, vol. 46, no. 5, pp. 1208–1220, May 1998.

[15] T. Liu, S. Boumaiza, and F. M. Ghannouchi, "Deembedding static nonlinearities and accurately identifying and modeling memory effects in wide-band RF transmitters," *IEEE Trans. Microw. Theory Tech.*, vol. 53, no. 11, pp. 3578–3587, Nov. 2005.

[16] J. Wood, M. LeFevre, D. Runton, J. C. Nanan, B. H. Noori, and P. H. Aaen, "Envelope-domain time series (ET) behavioural model of a doherty RFpower amplifier for system design," *IEEE Trans. Microw. Theory Tech.*, vol. 54, no. 8, pp. 3163–3171, Aug. 2006.

[17] G. Montoro, P. L. Gilabert, E. Bertran, A. Cesari, and D. D. Silveira, "A new digital predictive predistorter for behavioral power amplifier linearization," *IEEE Microw. Wireless Compon. Lett.*, vol. 17, no. 6, pp. 448–450, Jun. 2007.

[18] F. Mkaden and S. Boumaiza, "Extended hammerstein behavioral model using artificial neural networks," *IEEE Trans. Microw. Theory Tech.*, vol. 57, no. 4, pp. 745–751, Apr. 2009.

[19] A. Saleh, "Frequency-independent and frequency-dependent nonlinear models of TWT amplifiers," *IEEE Trans. Commun.*, vol. COM-29, no. 11, pp. 1715–1720, Nov. 1981.

[20] M. Abuelma'atti, "Frequency-dependent nonlinear quadrature model for TWT amplifiers," *IEEE Trans. Commun.*, vol. COM-32, no. 8, pp. 982–986, Aug. 1984.

[21] H. Ku, M. Mckinley, and J. S. Kenney, "Quantifying memory effects in RF power amplifiers," *IEEE Trans. Microw. Theory Tech.*, vol. 50, no. 12, pp. 2843–2849, Dec. 2002.

[22] C. Silva, A. Moulthrop, and M. Muha, "Introduction to polyspectral modeling and compensation techniques for wideband communications systems," in *58th ARFTG Conf. Dig.*, Nov. 2001, pp. 1–15.

[23] E. Ngoya, N. Le Gallou, J. M. Nébus, H. Burêt, and P. Reig, "Accurate RF and microwave system level modeling of wide band nonlinear circuits," in *IEEE MTT-S Int. Microw. Symp. Dig.*, Jun. 2000, pp. 79–82.

[24] A. Soury, E. Ngoya, and J. M. Nebus, "A new behavioral model taking into account nonlinear memory effects and transient behaviors in wideband SSPAs," in *IEEE MTT-S Int. Microw. Symp. Dig.*, Jun. 2002, pp. 853–856.

[25] A. Soury, E. Ngoya, J. M. Nebus, and T. Reveyrand, "Measurement based modeling of power amplifiers for reliable design of modern communication systems," in *IEEE MTT-S Int. Microw. Symp. Dig.*, Jun. 2003, pp. 795–798.

[26] D. Mirri, F. Filicori, G. Iuculano, and G. Pasini, "A nonlinear dynamic model for performance analysis of large-signal amplifiers in communication systems," *IEEE Trans. Instrum. Meas.*, vol. 53, no. 2, pp. 341–350, Apr. 2004.

[27] A. Soury and E. Ngoya, "A two-kernel nonlinear impulse response model for handling long term memory effects in RF and microwave solid state circuits," in *IEEE Int. Microw. Symp. Dig.*, Jun. 2006, pp. 1105–1108.

[28] V. Meghdadi, J. P. Cances, F. Chevallier, B. Rojat, and J. M. Dumas, "Modeling of solid state power amplifiers (SSPA) and validation by means of a system simulator," *Ann. Telecommun.*, vol. 53, no. 1–2, pp. 1/11–10/11, 1998.

[29] J. Vuolevi, T. Rahkonen, and J. Manninen, "Measurement technique for characterizing memory effects in RF power amplifiers," *IEEE Trans. Microw. Theory Tech.*, vol. 49, no. 8, pp. 1383–1389, Aug. 2001.

[30] P. Asbeck, H. Kobayashi, M. Iwamoto, G. Hanington, S. Nam, and L. E. Larson, "Augmented behavioral characterization for modeling the nonlinear response of power amplifiers," in *IEEE Int. Microw. Symp. Dig.*, Jun. 2002, pp. 135–138.

[31] P. Draxler, I. Langmore, T. P. Hung, and P. M. Asbeck, "Time domain characterization of power amplifiers with memory effects," in *IEEE MTT-S Int. Microw. Symp. Dig.*, Jun. 2003, pp. 803–806.

[32] J. C. Pedro, N. B. Carvalho, and P. M. Lavrador, "Modeling nonlinear behaviour of band-pass memoryless and dynamic systems," in *IEEE MTT-S Int. Microw. Symp. Dig.*, Jun. 2003, pp. 2133–2136.

[33] S. Boumaiza and F. M. Ghannouchi, "Thermal memory effects modeling and compensation in RF power amplifiers and predistortion linearizers," *IEEE Trans. Microw. Theory Tech.*, vol. 51, no. 12, pp. 2427–2433, Dec. 2003.

[34] C. Maziere, A. Soury, E. Ngoya, and J. M. Nébus, "A system level model of solid state amplifiers with memory based on a nonlinear feedback loop principle," in *35th EuMC Conf.*, Paris, France, 2005, pp. 853–856.

[35] Z. Madini, A. Bennadji, and E. Ngoya, "Identification and implementation of long term memory kernel in SSAs based on the compound dynamic Volterra structure for system level simulation," in *Asia-Pacific Microw. Conf.*, Bangkok, Thailand, 2007, pp. 2417–2420.

[36] J. S. Kenney and P. Fedorenk, "Identification of RF power amplifier memory effect origins using third order intermodulation distortion amplitude and phase asymmetry," in *IEEE MTT-S Int. Microw. Symp. Dig.*, Jun. 2006, pp. 1121–1124.

[37] J. Mazeau, R. Sommet, D. Caban-Chastas, E. Gatard, R. Quéré, and Y. Mancuso, "Behavioral thermal modeling for microwave power amplifier design," *IEEE Trans. Microw. Theory Tech.*, vol. 55, no. 11, pp. 2290–2297, Nov. 2007.

[38] J. Verspecht, J. Horn, L. Betts, D. Gunyan, R. Pollard, C. Gillease, and D. E. Root, "Extension of X-parameters to include long-term dynamic memory effects," in *IEEE Int. Microw. Symp. Dig.*, Jun. 2009, pp. 741–744.

[39] E. Ngoya, C. Quindroit, and J. M. Nébus, "Improvements on long term memory modeling in power amplifiers," in *IEEE MTT-S Int. Microw. Symp. Dig.*, Jun. 2009, pp. 1357–1360.

[40] C. Quindroit, E. Ngoya, A. Bennadji, and J. M. Nébus, "An orthogonal lookup-table decomposition for accurate IMD prediction in power amplifier with memory," in *IEEE Int. Microw. Symp. Dig.*, Jun. 2008, pp. 1437–1440.

[41] B. Gustavsen and A. Semlyen, "Rational approximation of frequency domain responses by vector fitting," *IEEE Trans. Power Delivery*, vol. 14, no. 3, pp. 1052–1061, Jul. 1999.

[42] B. Gustavsen, "Improving the pole relocating properties of vector fitting," *IEEE Trans. Power Delivery*, vol. 21, no. 3, pp. 1597–1592, Jul. 2006.
[43] Agilent Technologies, Santa Clara, CA, "The vector fitting web site," 1999. [Online]. Available: http://www.energy.sintef.no/Produkt/VECTFIT/index.asp
[44] Energy Sintef, Norway, "ADS project," 2000. [Online]. Available: http://eesof.tm.agilent.com/applications/amps-b.html

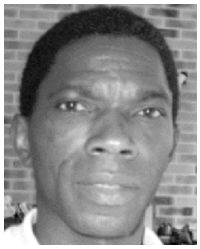

Edouard Ngoya received the Ph.D. degree in electronics from the University of Limoges, Limoges, France, in 1988.

He worked as an R&D Engineer with CAROLINE and RACAL-REDAC in 1988 and 1989. In 1990, he joined the French Centre National de la Recherche Scientifique (CNRS) as a Senior Researcher with XLIM–University of Limoges. He has initiated key circuit simulation and modeling techniques and contributed to the development of several ADE tools for nonlinear RF and microwave circuits. He cofounded Xpedion Design Systems and is author of the GoldenGate RFIC simulation tool by Agilent Technologies. His current research interests include full-chip RFIC simulation techniques, analog system bloc-level modeling, and PA linearization techniques.

Christophe Quindroit received the electrical engineering degree from the University of Nantes, Nantes, France, in 2005, and is currently working toward the Ph.D. degree from the XLIM Institute, University of Limoges, Limoges, France.

His research interests include the system modeling of power amplifiers and digital predistortion.

Jean-Michel Nebus was born in Bourganeuf, France, in 1963. He received the Ph.D. degree in electronics from the University of Limoges, Limoges, France, in 1988.

He was a Project Engineer with ALCATEL Space Industries, France. He is currently a Professor with the XLIM, University of Limoges. His main area of interest is nonlinear microwave device characterization and design.